PHYSICAL REVIEW D **95,** 122003 (2017)

Search for gravitational waves from Scorpius X-1 in the first Advanced LIGO observing run with a hidden Markov model

B. P. Abbott *et al.*[*]
(LIGO Scientific Collaboration and Virgo Collaboration)
(Received 12 April 2017; published 27 June 2017)

Results are presented from a semicoherent search for continuous gravitational waves from the brightest low-mass X-ray binary, Scorpius X-1, using data collected during the first Advanced LIGO observing run. The search combines a frequency domain matched filter (Bessel-weighted $\mathcal{F}$-statistic) with a hidden Markov model to track wandering of the neutron star spin frequency. No evidence of gravitational waves is found in the frequency range 60–650 Hz. Frequentist 95% confidence strain upper limits, $h_0^{95\%} = 4.0 \times 10^{-25}$, 8.3×10^{-25}, and 3.0×10^{-25} for electromagnetically restricted source orientation, unknown polarization, and circular polarization, respectively, are reported at 106 Hz. They are ≤ 10 times higher than the theoretical torque-balance limit at 106 Hz.

DOI: 10.1103/PhysRevD.95.122003

I. INTRODUCTION

Rotating neutron stars are a possible source of persistent, periodic gravitational radiation. The signal is expected at specific multiples of the neutron star spin frequency $f_\star$ [1]. Astrophysical models suggest that the radiation may be emitted at levels detectable by ground-based, long-baseline interferometers such as the Laser Interferometer Gravitational Wave Observatory (LIGO) and the Virgo detector [1–5]. A time-varying quadrupole moment can result from thermal [6,7] or magnetic [8–10] gradients, r-modes [11–14], or nonaxisymmetric circulation in the superfluid interior [15–18].

Accreting neutron stars in binary systems are important search targets because mass transfer spins up the star to $\gtrsim 10^2$ Hz and may simultaneously drive several quadrupole-generating mechanisms [19–23]. Moreover, it is observed that the distribution of spin frequencies of low-mass X-ray binaries (LMXBs) cuts off near 620 Hz [24], below the theoretical centrifugal break-up limit $\approx$1.4 kHz [25]. This has been explained by hypothesizing that the gravitational radiation-reaction torque balances the accretion torque [19,26,27], implying a relation between the X-ray flux and gravitational wave strain. Scorpius X-1 (Sco X-1), the most X-ray-luminous LMXB, is therefore a promising target for gravitational wave searches.

Initial LIGO achieved its design sensitivity over a wide band during LIGO Science Run 5 (S5) [28] and exceeded it during Science Run 6 (S6) [29]. The strain sensitivity of the next-generation Advanced LIGO interferometer is expected to improve ten-fold relative to Initial LIGO after several stages of upgrade [30]. In the first observation run (O1), from September 2015 to January 2016, the strain noise is three to four times lower than in S6 across the most sensitive band, between 100 Hz and 300 Hz, and $\sim$30 times lower around 50 Hz [31].

Four types of searches have been conducted for Sco X-1 using data collected by Initial LIGO and Advanced LIGO (O1). None of these searches reported a detection. First, a coherent search, using a maximum likelihood detection statistic called the $\mathcal{F}$-statistic [32], analyzed the most sensitive six-hour data segment from Science Run 2 (S2) and placed a 95% confidence strain upper limit at $h_0^{95\%} \approx 2 \times 10^{-22}$ for two bands, 464–484 Hz and 604–626 Hz [33]. Second, a directed, semicoherent analysis based on the sideband algorithm was conducted on a 10-day stretch of LIGO S5 data in the band 50–550 Hz and reported median strain upper limits of 1.3×10^{-24} and 8×10^{-25} at 150 Hz for arbitrary and electromagnetically restricted source orientations, respectively [34]. The sideband method sums incoherently the coherent $\mathcal{F}$-statistic power at frequency-modulated orbital sidebands and generates a new detection statistic called the $\mathcal{C}$-statistic [35,36]. Third, a directed version of the all-sky TwoSpect search [37] was applied to S6 data and the second and third Virgo science runs (VSR2 and VSR3, respectively), yielding low-frequency upper limits of $h_0^{95\%} \approx 2 \times 10^{-23}$ in the band from 20 Hz to 57.25 Hz [38]. Another search of S6 data was carried out using the subsequently improved TwoSpect method [39], spanning frequencies from 40 Hz to 2040 Hz and projected semi-major axis from 0.90 s to 1.98 s. It achieved a 95% confidence level random-polarization upper limit of $h_0^{95\%} = 1.8 \times 10^{-24}$ at 165 Hz [40]. Fourth, a directed version of the all-sky, radiometer search [41] was conducted on all 20 days of Science Run 4 (S4) data [42], and was later applied to two years of S5 data, yielding a 90% confidence root-mean-square strain upper limit of 7×10^{-25} at 150 Hz [43], which converts to $h_0^{90\%} = 2 \times 10^{-24}$ [44]. The same method was applied to O1 data, yielding a median frequency-dependent limit of

[*]Full author list given at end of the article.

$h_0^{90\%} = 6.7 \times 10^{-25}$ at the most sensitive detector frequencies between 130–175 Hz [45].

It is probable that the spin frequency of Sco X-1 wanders stochastically under the fluctuating action of the hydromagnetic torque exerted by the accretion flow [46–48]. Search methods that scan templates without guidance from a measured ephemeris are compromised because of spin wandering; for example, the sideband search is restricted to a 10-day stretch of data in Ref. [34], so the signal power does not leak into adjacent frequency bins. Hidden Markov model (HMM) tracking offers a powerful strategy for detecting a spin-wandering signal [49]. A HMM relates a sequence of observations to the most probable Markov sequence of allowed transitions between the states of an underlying, hidden state variable (here the gravitational wave signal frequency f_0) [50]. It can track f_0 over the total observation time T_{obs} by incoherently combining segments with duration $T_{\mathrm{drift}} = 10$ d of the output from a maximum-likelihood, coherent matched filter, improving the sensitivity by a factor $\approx (T_{\mathrm{obs}}/T_{\mathrm{drift}})^{1/4}$ relative to a single segment.

In this paper, we combine the sideband algorithm with a HMM and apply it to Advanced LIGO O1 data. Specifically, we carry out a directed search for Sco X-1 in the band 60–650 Hz. No evidence of a gravitational-wave signal is found. Frequentist 95% confidence strain upper limits of $h_0^{95\%} = 4.0 \times 10^{-25}$, 8.3×10^{-25}, and 3.0×10^{-25} are derived at 106 Hz, for electromagnetically restricted source orientation, unknown polarization, and circular polarization, respectively. The paper is organized as follows. In Sec. II, we briefly review the search algorithm. In Sec. III, we discuss the astrophysical parameters of the source, search procedure, detection threshold and estimated sensitivity. Results of the search, including veto output, candidate follow-up, and gravitational wave strain upper limits are presented in Sec. IV. We discuss the torque-balance upper limit in Sec. V and conclude with a summary in Sec. VI.

II. METHOD

In this section we briefly introduce the HMM formulation of frequency tracking and the Viterbi algorithm for solving the HMM in Sec. II A and Appendixes A and B, respectively. A matched filter appropriate for a continuous-wave source in a binary is reviewed in Sec. II B. A full description of the method can be found in Ref. [49].

A. HMM tracking

A HMM is a finite state automaton, in which a hidden (unobservable) state variable $q(t)$ transitions between values from the set $\{q_1, \ldots, q_{N_Q}\}$ at discrete times $\{t_0, \ldots, t_{N_T}\}$, while an observable state variable $o(t)$ transitions between values from the set $\{o_1, \ldots, o_{N_O}\}$. The probability that $q(t)$ jumps from state q_i to state q_j is given by the transition matrix $A_{q_i q_j}$. The likelihood that the hidden state q_i gives rise to the observation o_j is given by the emission probability $L_{o_j q_i}$. In this application, we map the discrete hidden states one-to-one to the frequency bins in the output of a frequency-domain estimator $G(f)$ (see Sec. II B) computed over an interval of length T_{drift}, with bin size $\Delta f_{\mathrm{drift}} = 1/(2T_{\mathrm{drift}})$. The procedure for choosing T_{drift} is described in Appendix A.

For a Markov process, the probability that the hidden path $Q = \{q(t_0), \ldots, q(t_{N_T})\}$ gives rise to the observed sequence $O = \{o(t_0), \ldots, o(t_{N_T})\}$ is given by

$$P(Q|O) = L_{o(t_{N_T})q(t_{N_T})} A_{q(t_{N_T})q(t_{N_T-1})} \cdots L_{o(t_1)q(t_1)} \times A_{q(t_1)q(t_0)} \Pi_{q(t_0)}, \tag{1}$$

where Π_{q_i} denotes the prior (see Appendix A). The classic Viterbi algorithm [51] provides a recursive, computationally efficient route to computing $Q^*(O)$, the path that maximizes $P(Q|O)$. The steps in the algorithm are specified in Appendix B; the number of operations is of order $(N_T + 1)N_Q \ln N_Q$ [50]. In this paper, we define a detection score S, such that the log likelihood of the optimal Viterbi path equals the mean log likelihood of all paths plus S standard deviations, viz.

$$S = \frac{\ln \delta_{q^*}(t_{N_T}) - \mu_{\ln\delta}(t_{N_T})}{\sigma_{\ln\delta}(t_{N_T})} \tag{2}$$

with

$$\mu_{\ln\delta}(t_{N_T}) = N_Q^{-1} \sum_{i=1}^{N_Q} \ln \delta_{q_i}(t_{N_T}) \tag{3}$$

and

$$\sigma_{\ln\delta}(t_{N_T})^2 = N_Q^{-1} \sum_{i=1}^{N_Q} [\ln \delta_{q_i}(t_{N_T}) - \mu_{\ln\delta}(t_{N_T})]^2, \tag{4}$$

where $\delta_{q_i}(t_{N_T})$ denotes the maximum probability of the path ending in state q_i $(1 \le i \le N_Q)$ at step N_T (see Appendix B), and $\delta_{q^*}(t_{N_T})$ is the likelihood of the optimal Viterbi path, i.e., $P[Q^*(O)|O]$.

B. Matched filter: Bessel-weighted $\mathcal{F}$-statistic

The emission probability $L_{o(t)q_i}$ is computed from a frequency-domain estimator $G(f)$ as described in Appendix A. In the context of continuous-wave searches, $G(f)$ is a matched filter. The optimal matched filter for a biaxial rotor with no orbital motion is the maximum-likelihood $\mathcal{F}$-statistic [32], which accounts for the rotation of the Earth and its orbit around the Solar System barycenter (SSB). When the source orbits a binary companion,

TABLE I. Electromagnetically observed parameters (top half) and search parameters (bottom half) for Sco X-1. The uncertainties are at the 1σ confidence level.

Observed parameter	Symbol	Value	Reference
Right ascension	α	16 h 19 m 55.0850 s	[55]
Declination	δ	$-15°38'24.9''$	[55]
X-ray flux	F_X	4×10^{-7} erg cm^{-2} s^{-1}	[56]
Orbital period	P	68023.70496 ± 0.0432 s	[57]
Projected semimajor axis	a_0	1.44 ± 0.18 s	[58]
Polarization angle	ψ	$234 \pm 3°$	[59]
Inclination angle	ι	$44 \pm 6°$	[59]
Search parameter	**Symbol**	**Search range**	**Resolution**
Frequency	f_0	60–650 Hz	5.787037×10^{-7} Hz
Projected semimajor axis	a_0	0.361–3.249 s	0.01805 s

the gravitational-wave signal frequency is modulated due to the orbital Doppler effect [35,36,52]. The $\mathcal{F}$-statistic power is distributed into approximately $M = 2m + 1$ orbital sidebands with $m = \mathrm{ceil}(2\pi f_0 a_0)$, separated in frequency by $1/P$, where f_0 is the intrinsic gravitational-wave frequency, a_0 is the light travel time across the projected semimajor axis of the orbit, P is the orbital period, and $\mathrm{ceil}(x)$ denotes the smallest integer greater than or equal to x. For a Keplerian orbit with zero eccentricity, the gravitational wave strain can be expanded in a Jacobi-Anger series as [49,53]

$$h(t) \propto \sum_{n=-\infty}^{\infty} J_n(2\pi f_0 a_0) \cos[2\pi(f_0 + n/P)t], \quad (5)$$

where $J_n(z)$ is a Bessel function of order n of the first kind. The mathematical form of Eq. (5) suggests a Bessel-weighted $\mathcal{F}$-statistic as the matched filter $G(f)$ for a biaxial rotor in a binary system, which can be expressed as the convolution [49]

$$G(f) = \mathcal{F}(f) \otimes B(f), \quad (6)$$

where $B(f)$ is given by

$$B(f) = \sum_{n=-(M-1)/2}^{(M-1)/2} [J_n(2\pi f a_0)]^2 \delta(f - n/P). \quad (7)$$

Compared to the $\mathcal{C}$-statistic, used in a previously published sideband search for Sco X-1 [36,49], where the factor $[J_n(2\pi f a_0)]^2$ in Eq. (7) is replaced by unity, the Bessel-weighted matched filter recovers approximately $\sqrt{2}$ times more signal. It marshals more power into a single bin, producing a distinct spike with shoulders instead of the relatively flat onion-dome peak produced by the $\mathcal{C}$-statistic. These characteristics facilitate Viterbi tracking (see Sec. IV A in Ref. [49] for details). We leverage the existing, efficient, thoroughly tested $\mathcal{F}$-statistic software infrastructure in the LSC Algorithm Library Applications (LALApps)[1] to compute $\mathcal{F}(f)$ in Eq. (6) [54].

III. IMPLEMENTATION

In this section we introduce the electromagnetically measured source parameters of Sco X-1 (Sec. III A) and describe the workflow of the pipeline (Sec. III B), detection threshold (Sec. III C), and search sensitivity (Sec. III D).

A. Sco X-1 parameters

The sky position (α, δ), orbital elements (a_0, P), and orientation angles (ι, ψ) of Sco X-1 have been measured electromagnetically to various degrees of accuracy. The values and 1σ (68%) confidence level uncertainties are quoted in the top half of Table I.

The published uncertainty in the orbital period, $\Delta P = 0.0432$ s [57], restricts the coherent observation time to $T_{\mathrm{drift}} \leq 50$ d [34,36]. Hence, it is safe to take a single, fixed P value when evaluating the $\mathcal{F}$-statistic, given that the coherent data stretches we analyze are limited to 10 d (20 d for follow-up; see Sec. IV A 4). The published uncertainty in the projected semimajor axis, inferred from the measured orbital velocity, is $\Delta a_0 = 0.18$ s [58]. In the previous S5 sideband search, it was demonstrated that taking a single, fixed a_0 value does not impact search sensitivity given this published uncertainty [34,36]. However, recent unpublished research has revised the range of a_0 upwards to $0.36\mathrm{s} \leq a_0 \leq 3.25$ s. This is because the orbital velocity is difficult to measure electromagnetically, and the previous measurement is based on searching for the optimal centre of symmetry in the accretion disk emission, yielding an estimated velocity of 40 ± 5 km s^{-1} [58]. The preliminary results from the more recent study, which uses Doppler tomography measurements and Markov Chain Monte-Carlo analysis for the velocity, show that the constraint on the orbital velocity is weaker, corresponding to a

[1] https://www.lsc-group.phys.uwm.edu/daswg/projects/lalapps/.

range from 10 kms^{-1} to 90 kms^{-1} [60,61]. It is shown in Sec. IV B of Ref. [49] that if the true value of a_0 differs from the estimated a_0 by 10%, it would produce an uncertainty in the estimated frequency of ≈0.001 Hz. Moreover, the log likelihood of the optimal path decreases by ∼50% if the true value of a_0 differs from the estimated a_0 by 25%. We search over the wider, unpublished range of a_0 with a resolution of 0.01805 s in order to preserve sensitivity. The orientation angles ι and ψ are measured from the position angle of the Sco X-1 radio jets on the sky, assuming that the rotation axis of the neutron star is perpendicular to the accretion disk. In the previously published sideband search, two orientation priors are considered: (1) uniform distributions of $\cos\iota$ and ψ; and (2) distributions peaked around the observed values in the top half of Table I.

The parameter space covered by the search is defined in the bottom half of Table I. We assume uniform priors on both f_0 and a_0.

B. Workflow

The search is parallelized into 1-Hz sub-bands to assist with managing the relatively large volume of data involved. The sub-bands must be narrow enough that we can replace f with the mean value $\bar{f}$ in each sub-band to a good approximation, in order to avoid recalculating $B(f)$ in every frequency bin. The sub-bands must also be wide enough to contain the width of the matched filter. Sub-bands of 1 Hz satisfy both of these requirements and were also adopted in the S5 sideband search [34].

The flow chart in Fig. 1 summarizes the procedural steps in the search pipeline. Firstly, the 30-min short Fourier transforms (SFTs) constituting the whole observation are divided into N_T blocks, each of duration $T_{\mathrm{drift}} = 10$ d. In each 1-Hz sub-band, the $\mathcal{F}$-statistic is computed for each block at the known sky location of the source. Next we compute the Bessel-weighted $\mathcal{F}$-statistic $G(f)$ from Eqs. (6) and (7), taking a_0 and P as inputs; that is, $G(f)$ is computed in N_{f_0} frequency bins for each of the N_T blocks. Theoretically, the HMM hidden state variable is two-dimensional because we search over f_0 and a_0. In practice, a_0 varies imperceptibly on the time scale T_{obs}, so the algorithm is equivalent to multiple, independent, one-dimensional HMM searches over f_0 on a grid of a_0 values. The detection score and corresponding optimal Viterbi path are recorded in each 1-Hz sub-band. We evaluate the detection scores to identify candidates, judge whether or not they come from instrumental artifacts via a well-defined hierarchy of vetoes, and claim a detection or compute strain upper limits for sub-bands without candidates.

C. Threshold

We determine the Viterbi score threshold S_{th} for a given false alarm rate α_{f} through Monte-Carlo simulations, such that searching data sets containing pure noise yields a

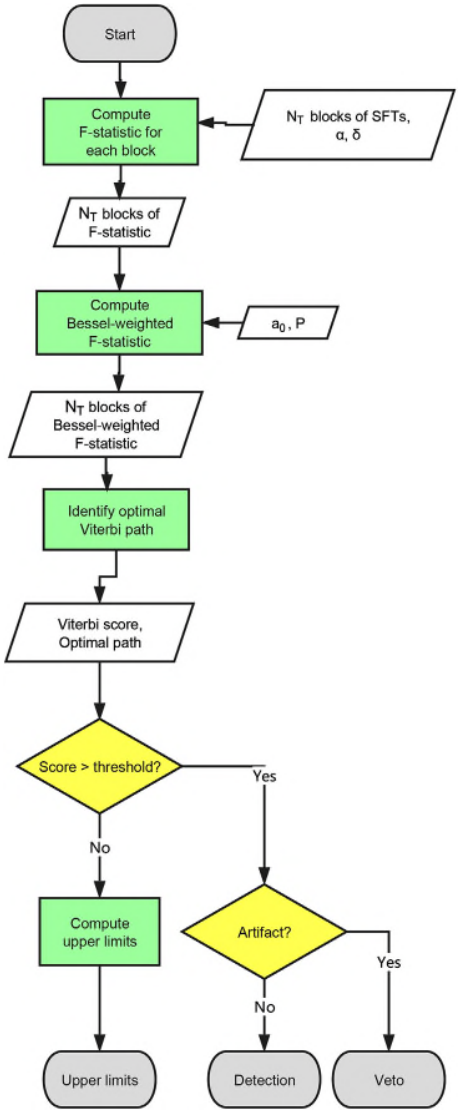

FIG. 1. Flowchart of the pipeline in each 1-Hz sub-band.

fraction α_{f} of positive detections with $S > S_{\mathrm{th}}$. SFTs containing pure Gaussian noise are generated for seven 1-Hz sub-bands, starting at 55 Hz, 155 Hz, 255 Hz, 355 Hz, 455 Hz, 555 Hz, and 650 Hz, with the same single-sided power spectral density (PSD) $S_h(f)$ as actual O1 data and with $T_{\mathrm{obs}} = 130$ d. Searches are repeated for 100 noise realizations in each 1-Hz sub-band following the recipe in Fig. 1. We track 161 a_0 values from 0.361 s to 3.249 s, with resolution 0.01805 s, as for a real search. We find that the results depend weakly on the sub-bands: the mean $\langle S\rangle$ varies from 6.48 to 6.59, and the standard deviation σ_S varies from 0.24 to 0.33. Combining the 700 realizations yields $S_{\mathrm{th}} = 7.34$ for $\alpha_{\mathrm{f}} = 1\%$.

To check the influence of non-Gaussian noise on S_{th}, we choose three 1-Hz sub-bands, starting at 157 Hz, 355 Hz, and 635 Hz, in O1 interferometer data and repeat the search for real noise. As we have no means of generating multiple,

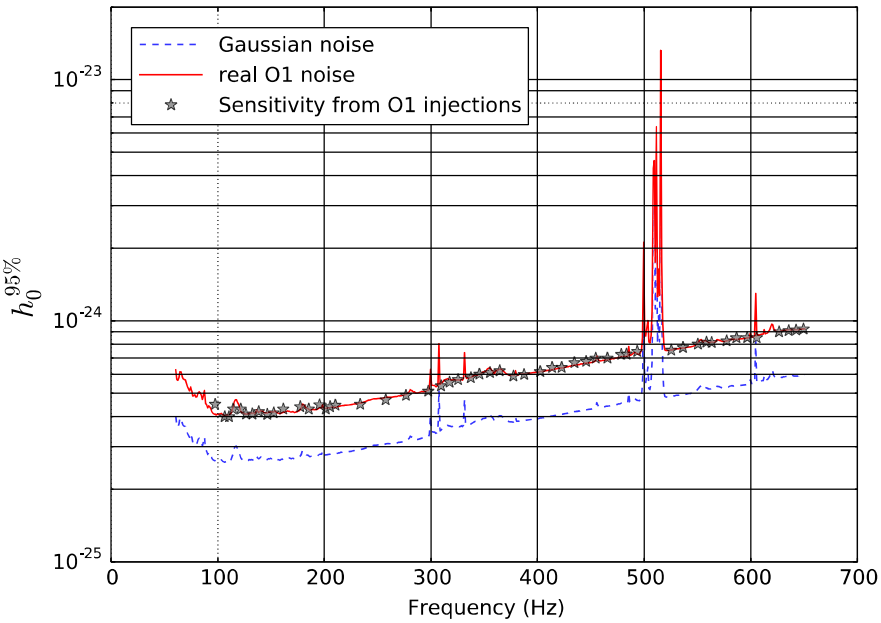

FIG. 2. Characteristic wave strain for 95% detection efficiency, $h_0^{95\%}$, versus frequency (Hz) from Monte-Carlo simulations. Signals are injected with a restricted inclination angle $\cos\iota_{\rm inj} \approx 0.7193$. Blue dashed curve: $h_0^{95\%}$ from Gaussian noise with $S_h(f)$ evaluated from the nominal O1 PSD and $T_{\rm obs} = 130$ d. Gray stars: $h_0^{95\%}$ from injections into real O1 interferometer data in 53 1-Hz sub-bands. Red solid curve: $h_0^{95\%}$ in real O1 noise, corrected for duty cycle and nongaussianity by multiplying the blue dashed curve by a factor $\kappa = 1.56$. The red solid curve overlaps substantially with the gray stars.

random, real-noise realizations from scratch, we take 100 different sky locations as background noise realizations. We find that $\langle S\rangle$ and σ_S range from 6.36 to 6.38 and 0.27 to 0.34, respectively. These results match the output from Gaussian noise simulations to better than ~3%, as does $S_{\rm th}$. Hence, we set $S_{\rm th} = 7.34$ in the forthcoming analysis described in Sec. IV.

In the follow-up procedures in Sec. IV, we search a subset of the data either from a single interferometer with $T_{\rm obs} = 130$ d $= 13T_{\rm drift}$ or two interferometers with $T_{\rm obs} = 60$ d $= 6T_{\rm drift}$. To check the validity of $S_{\rm th} = 7.34$ when searching a subset of the data, we run 400 trials of Gaussian noise simulations using data generated for a single interferometer with $T_{\rm obs} = 130$ d or two interferometers with $T_{\rm obs} = 60$ d. The resulting $S_{\rm th}$ remains the same overall, and $\langle S\rangle$ and σ_S range from 6.44 to 6.50 and 0.27 to 0.30, respectively, matching the output in the simulations with two interferometers and $T_{\rm obs} = 130$ d to better than ~3%. Hence, we keep $S_{\rm th} = 7.34$ fixed for the follow-up procedures in Sec. IV.

D. Sensitivity

Given the threshold $S_{\rm th}(\alpha_{\rm f} = 1\%) = 7.34$, we evaluate the characteristic wave strain yielding 95% detection efficiency (i.e., 5% false dismissal rate), denoted by $h_0^{95\%}$, through Monte-Carlo simulations with signals injected into Gaussian noise. The simulations are performed between 155–156 Hz, where the detectors are most sensitive, with $T_{\rm obs} = 130$ d, $T_{\rm drift} = 10$ d, $N_T = 13$, $\sqrt{S_h} = 1 \times 10^{-23}$ Hz$^{-1/2}$, and source parameters copied from Table I. We choose $T_{\rm obs} = 130$ d to equal the duration of O1. The parameters $f_{0\rm inj}$, $a_{0\rm inj}$, $\cos\iota_{\rm inj}$, and $\psi_{\rm inj}$ are randomly chosen with a uniform distribution within the ranges 155.34565530–155.3456847 Hz, 0.36–3.25 s, 0.712107–0.726493, and $0 - 2\pi$rad, respectively. We obtain $h_0^{95\%} = 3 \times 10^{-25}$ for electromagnetically restricted orientation by assuming $\iota \approx 44°$ [59]. In reality, the signal-to-noise ratio scales in proportion to $h_0^{\rm eff}$, given by

$$h_0^{\rm eff} = h_0 2^{-1/2}\{[(1+\cos^2\iota)/2]^2 + \cos^2\iota\}^{1/2}, \quad (8)$$

rather than h_0 [32,62]. Hence, we can convert the limiting wave strain to $h_0^{\rm eff,95\%} \approx 0.74 h_0^{95\%}$ using the value $\iota = 44°$. For $T_{\rm obs}$ fixed, we expect

$$h_0^{95\%} \propto S_h^{1/2} f_0^{1/4}. \quad (9)$$

The latter scaling is verified by a group of injections in three other frequency bands (55–56 Hz, 355–356 Hz, and 649–650 Hz). Evaluating $S_h(f)$ from the O1 PSD, we plot $h_0^{95\%}$ versus f_0 as the blue dashed curve in Fig. 2, which represents the 95% detection efficiency curve in Gaussian noise simulations.

In practice, interferometer noise is non-Gaussian, and $T_{\rm obs}$ is less than 130 d (duty cycle ≈ 60%). To correct for this, we pick 53 1-Hz sub-bands, run 3000 injections in real

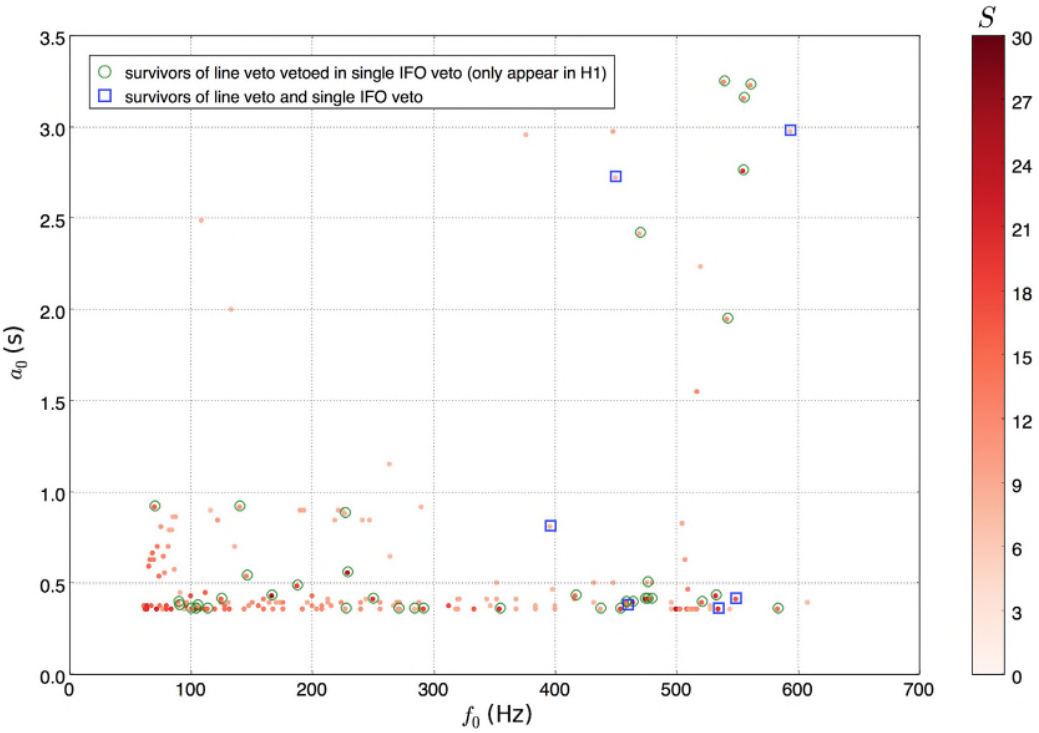

FIG. 3. First-pass candidates and survivors of the known line veto and single interferometer veto. The detection score S in each 1-Hz sub-band is plotted as a function of f_0 and a_0 as estimated by the HMM. Each red dot stands for one candidate with $S > S_{\rm th} = 7.34$. The color of the dots scales with S (see color bar at right). Red dots without green circles or blue squares are vetoed due to contamination by known instrumental lines. Candidates are marked by green circles if they are detected with higher S in H1 than the original score but not detected in L1. Green circles are vetoed (category A in Table III). None of the candidates is detected with higher S in L1 than the original score while not being detected in H1. Candidates marked by blue squares survive both the known line veto and the single interferometer veto and require further follow-up.

O1 interferometer data, and compare the resulting $h_0^{95\%}$ to the blue dashed curve in Fig. 2. The injected signal parameters are chosen in the same way as in the Gaussian noise simulation. In each sub-band tested, the resulting $h_0^{95\%}$ values from real O1 injections are plotted as gray stars in Fig. 2. The correction factor κ in each 1-Hz sub-band is defined as $h_0^{95\%}$, as marked by the gray star, divided by the value read off the blue dashed curve. The correction factors in the 53 sub-bands fluctuate weakly, with mean $\langle\kappa\rangle = 1.56$ and standard deviation $\sigma_\kappa = 0.03$. We therefore apply the same $\kappa = 1.56$ across the full search and adjust the blue dashed curve to give the red solid curve in Fig. 2. The latter represents the characteristic wave strain for 95% detection efficiency as a function of frequency in real O1 data. We find that 2846 out of the 3000 O1 injections are detected with $S > S_{\rm th}$, yielding a detection rate of 94.87%, consistent with the targeted detection efficiency.

IV. O1 ANALYSIS

In this section, we analyze data from the O1 observing run extending from September 12, 2015 to January 19, 2016 UTC (GPS time 1126051217 to 1137254417). The data are divided into 13 blocks, with $T_{\rm drift} = 10$ d, and fed into the HMM tracker described in Secs. II and III.

Narrowband, instrumental noise lines (e.g., power line at 60 Hz, beam splitter violin mode, electronics, mirror suspension, calibration) and their harmonics can obscure astrophysical continuous-wave signals. At low frequencies between 25 Hz and 60 Hz, there are at least six known lines in each 1-Hz sub-band, and $\approx 2/3$ of the sub-bands contain more than 15 lines. Hence, we do not search below 60 Hz because the optimal paths returned by the HMM are dominated by difficult-to-model noise. The sensitivity of the method degrades as the width $4\pi a_0 f_0/P$ of the matched filter increases (see Sec. II B). We terminate the search arbitrarily at $f_0 = 650$ Hz to keep $4\pi a_0 f_0/P$ below ≈ 0.4 Hz, which is almost half the width of a sub-band.

We record the first-pass candidates identified by the search in Fig. 3. We then sift them through a systematic hierarchy of vetoes as follows: (1) known instrumental line veto (Sec. IV A 1), (2) single interferometer veto (Sec. IV A 2), (3) $T_{\rm obs}/2$ veto (Sec. IV A 3), and (4) $T_{\rm drift}$ veto (Sec. IV A 4). The safety verification of the four-step veto procedure is described in Sec. IV B. Table II lists the numbers of candidates surviving after each veto. No candidate survives all the vetoes, so we set upper limits on h_0. The strain upper limits are discussed in Sec. IV C.

TABLE II. Number of candidates surviving each veto.

Veto	Number
First pass	180
After line veto	44
After single IFO veto	6
After half $T_{\rm obs}$ veto	2
After longer $T_{\rm drift}$ veto	0

A. Vetoes

1. Known line veto

First-pass candidates with $S > S_{\rm th} = 7.34$ (red dots) are plotted in Fig. 3 as a function of f_0 and a_0 as estimated by the HMM. Each dot stands for a candidate in a 1-Hz sub-band. The color of a dot indicates its associated S value (higher S in darker shade). The HMM returns an optimal path $f_0(t)$ whose wandering is too slight to be discerned visually in Fig. 3. We take f_0 to equal the arithmetic mean of the min $f_0(t)$ and max $f_0(t)$ in the plot.

A candidate is vetoed if $f_0(t)$ satisfies $|f_0(t) - f_{\rm line}| < 4\pi a_0 f_0/P$ *anywhere* on the path, where $f_{\rm line}$ is the frequency of a known instrumental noise line. We find that the line veto excludes 75% of the candidates. The 44 survivors are marked by green circles or blue squares in Fig. 3. (The distinction between the green and blue symbols is discussed below.) One immediately notices that most of the red dots appear at $a_0 \lesssim 0.5$ s for all f_0. This is because a narrower matched filter produces a higher score when it encounters a narrow noise line. A noise line that produces high $\mathcal{F}$-statistic values concentrated in a handful of frequency bins spreads out when convolved with the matched filter in Eq. (7) and contributes to every Bessel-weighted $\mathcal{F}$-statistic bin in the band $|f_0(t) - f_{\rm line}| < 4\pi a_0 f_0/P$. The Viterbi score computed from the log likelihood of the optimal path is normalized by the standard deviation of all the log likelihoods in a 1-Hz sub-band. It is higher if the $\mathcal{F}$-statistic output containing a noise line is convolved with a narrower matched filter (i.e., smaller a_0) because the $\mathcal{F}$-statistic–processed noise-line power is dispersed into fewer orbital sidebands. The plot confirms that most vetoed candidates have $a_0 \lesssim 0.5$ s.

Instrumental lines are picked up readily by the HMM, rendering any astrophysical signal invisible in the relevant 1-Hz sub-band. One might seek to improve the search by notching out the instrumental lines first, before applying the HMM to the rest of the sub-band. However, O1 lines cluster closely below 90 Hz and near 300 Hz and 500 Hz, fragmenting the uncontaminated bands. It is onerous to circumvent the fragmentation, so we postpone this improvement to future searches, when better interferometer sensitivity will warrant the extra effort. In this search, we do not report results in a 1-Hz sub-band if the optimal path intersects any instrumental line. In total, 136 out of 591 1-Hz sub-bands are removed in this way.

2. Single interferometer veto

We now examine the 44 candidates surviving the known line veto by searching data from H1 and L1 separately. The sensitivities of the two interferometers during O1 are comparable, implying either that an astrophysical signal should appear in both detectors if it is strong enough or that it cannot be detected in either detector but can be seen after combining data from both. In contrast, a candidate is more likely a noise artifact originating in a single detector if it is detected in one detector with higher S than the original combined score $S_\cup$, while the other detector yields $S < S_{\rm th}$.

We can categorize survivors of the known line veto in Sec. IV A 1 into four classes presented in Table III.

Category A.—Only one detector yields $S > S_{\rm th}$, equal to or higher than $S_\cup$, and the frequency estimated from the detector with $S \geq S_\cup$ is approximately equal to that obtained by combining both, with an absolute discrepancy less than $2\pi a_{0\cup} f_{0\cup}/P$, where $a_{0\cup}$ and $f_{0\cup}$ are the a_0 and f_0 estimated using both detectors. Typically, we find that the absolute discrepancy is less than 0.01 Hz, even smaller than $2\pi a_{0\cup} f_{0\cup}/P$. Any astrophysical signal that is too weak to yield $S > S_{\rm th}$ in one detector is unavoidably obscured by the undocumented noise artifact in the other detector. Hence, we veto candidates in category A.

Category B.—Only one detector yields $S > S_{\rm th}$, equal to or higher than $S_\cup$, but the optimal path from the detector with $S \geq S_\cup$ occurs at f_0 with $|f_0 - f_{0\cup}| \geq 2\pi a_{0\cup} f_{0\cup}/P$ (denoted by $f_0 \neq f_{0\cup}$ in Table III). It is possible that a real signal only shows up at $f_{0\cup}$ after combining data from two

TABLE III. Actions to be taken for survivors of the known line veto in Sec. IV A 1 according to the score S and the estimated frequency f_0 from each single detector. $S_\cup$ and $f_{0\cup}$ stand for the score and estimated frequency yielded by the original search combining two detectors.

Category	Score in one detector S	Estimated frequency in one detector f_0	Action
A	$S \geq S_\cup$ in one detector but $S < S_{\rm th}$ in the other	$f_0 \approx f_{0\cup}$ where $S \geq S_\cup$	Veto
B	$S \geq S_\cup$ in one detector but $S < S_{\rm th}$ in the other	$f_0 \neq f_{0\cup}$ where $S \geq S_\cup$	Keep
C	$S \geq S_{\rm th}$ in both detectors		Keep
D	$S < S_{\rm th}$ in both detectors		Keep

TABLE IV. Candidates surviving both the known line veto and the single interferometer veto. The table lists the sub-band where the candidate is found (column 1), the estimated frequency f_0 quoted as the arithmetic mean of the minimum and the maximum frequencies ($f_{\min}$ and $f_{\max}$) in the optimal HMM path (column 2), the number of frequency bins (Δf_{drift}) between $f_{\max}$ and $f_{\min}$ (column 3), the estimated a_0 (column 4), the original score $S_{\cup}$ yielded by searching the whole data set (column 5), and the scores from searching the first and second half of the data separately (columns 6 and 7). The resolutions of f_0 and a_0 are 5.787037×10^{-7} Hz and 0.01805 s, respectively. The candidates marked with an asterisk survive the manual veto in Sec. IV A 3 and require further follow-up.

Sub-band (Hz)	f_0 (Hz)	$f_{\max} - f_{\min}$ (Δf_{drift})	a_0 (s)	$S_{\cup}$	$S_{1\,\text{st half}}$	$S_{2\,\text{nd half}}$
395–396	395.8561536	3	0.81	8.05153	6.55545	9.13679
449–450*	449.8116935	3	2.73	7.38701	6.46122	6.50190
459–460	459.5557459	6	0.38	12.76130	14.61070	6.30887
534–535	534.3625717	4	0.36	20.18630	20.53770	6.97788
548–549	548.9457104	7	0.42	16.68650	18.39020	6.46258
593–594*	593.7716675	1	2.98	7.40397	6.17976	5.88553

detectors. Hence, we keep candidates in category B for follow-up.

Category C.—Both detectors yield $S \geq S_{\text{th}}$. The candidate may come either from noise or from a real signal registering strongly in both detectors. Hence, we keep candidates in category C for follow-up.

Category D.—Both detectors yield $S < S_{\text{th}}$ even though we have $S_{\cup} \geq S_{\text{th}}$. A real signal may be too weak to register in either detector individually but rises above the noise when the two detectors are combined. Hence, we keep candidates in categories D for further examination.

Among the 44 candidates surviving the line veto, 38 in total are vetoed. They are marked by green circles in Fig. 3. All of them only appear in H1. The remaining six candidates marked by blue squares need to be examined further manually. Four of them show higher scores in H1 and $S < S_{\text{th}}$ in L1, but the estimated f_0 from H1 is different from that obtained by combining both detectors, falling into category B in Table III. Two candidates, in the sub-bands 449–450 Hz and 593–594 Hz, fall into category D in Table III, with $S < S_{\text{th}}$ in both H1 and L1.

3. $T_{\text{obs}}/2$ veto

We now divide the observing run into two halves: September 12, 2015 to November 20, 2015 UTC (GPS time 1126051217 to 1132020365) and November 20, 2015 to January 19, 2016 UTC (GPS time 1132020366 to 1137254417). We search the halves separately in the six 1-Hz sub-bands containing the veto survivors listed in Table IV, combining data from two interferometers. Similar to the criteria listed in Sec. IV A 2, we veto a candidate if it appears in one half, with $S \geq S_{\cup}$, but does not appear in the other half, and if the estimated f_0 value is approximately equal to the original value.

The three candidates near 459 Hz, 534 Hz, and 548 Hz appear in the first half with higher S but not in the second half. The candidate near 395 Hz appears in the second half with higher S but not in the first half. Each one of them is detected in the first or second half at a frequency approximately equal to the original estimated f_0 with absolute discrepancy less than 0.01 Hz.

In sub-bands 449 Hz and 593 Hz, neither of the two halves yields $S > S_{\text{th}}$. These two candidates are marked by an asterisk in Table IV and require further follow-up.

4. T_{drift} veto

In general, we can categorize any survivors of the $T_{\text{obs}}/2$ veto into four groups with reference to the optimal paths detected in the original search. The groups are defined in Table V. We expect S to increase as the block length T_{drift} increases, as long as T_{drift} remains shorter than the intrinsic spin-wandering time scale. One could therefore imagine vetoing a candidate whose optimal Viterbi path does not wander significantly if increasing T_{drift} up to the observed wandering time scale does not increase S. However, based on our experience analyzing injections (see Sec. IV B), we adopt a more conservative approach to reduce the false dismissal rate from this veto step. Specifically, we veto a candidate whose optimal Viterbi path does not wander significantly if increasing T_{drift} up to the observed wandering time scale yields $S < S_{\text{th}}$ (i.e., S drops below threshold) and the optimal paths returned for the two T_{drift} values do not match. For a candidate whose optimal Viterbi path does wander significantly, we do not expect S to increase with

TABLE V. Subsequent actions to be taken for survivors of the vetoes in Sec. IV A 1–IV A 3 according to the amount of spin wandering and S-versus-T_{drift} trend observed by the HMM.

	Higher S with longer T_{drift}	Lower S with longer T_{drift}
Low spin wandering	Follow-up with more sensitive method	Veto
High spin wandering	Unlikely to happen	Follow-up with more sensitive method guided by observed Viterbi path

TABLE VI. Final-step follow-up with longer $T_{\mathrm{drift}} = 20$ d in two 1-Hz sub-bands containing the survivors from Sec. IV A 3. The top and bottom halves of the table correspond to $T_{\mathrm{drift}} = 10$ d and 20 d, respectively. The estimated f_0 is quoted as the arithmetic mean of min $f_0(t)$ and max $f_0(t)$ for the optimal Viterbi path. The follow-up score S with $T_{\mathrm{drift}} = 20$ d is always below $S_{\mathrm{th}} = 7.34$ and lower than the original score. The resolutions of a_0 and f_0 are 0.01805 s and 5.787037×10^{-7} Hz, respectively for both $T_{\mathrm{drift}} = 10$ d and 20 d.

T_{drift}	Quantity	449–450 Hz	593–594 Hz
10 d	S	7.38701	7.40397
	f_0 (Hz)	449.8116936	593.7716675
	a_0 (s)	2.73	2.98
20 d	S	6.93366	6.93900
	f_0 (Hz)	449.7891863	593.6174193
	a_0 (s)	1.70	1.79

T_{drift} if the intrinsic spin-wandering time scale is effectively shorter than T_{drift} already. Indeed, it is reasonable for a strongly wandering signal to disappear when tracked with longer T_{drift}. On the rare occasion when this does happen, the candidate is likely to be a noise artifact. Candidates surviving the T_{drift} veto need to be followed up with more sensitive search pipelines (e.g., cross-correlation [63]).

In this search, the two survivors marked with asterisks in Table IV do not display strong spin wandering; they drift within three and one f_0 bins (see Fig. 5 in Appendix C). Hence, we expect S to increase at approximately the same f_0 as T_{drift} increases all the way up to T_{obs}. In fact, we find that it suffices to consider $T_{\mathrm{drift}} = 20$ d. The original and follow-up results are recorded in Table VI. For $T_{\mathrm{drift}} = 20$ d, no path is detected with $S > S_{\mathrm{th}}$ at sub-bands 449 Hz and 593 Hz. The optimal Viterbi paths returned from $T_{\mathrm{drift}} = 10$ d and 20 d are different in each of the two sub-bands, with an absolute discrepancy $\gtrsim 0.02$ Hz and $\gtrsim 1.03$ s for estimated f_0 and a_0, respectively. Normally the absolute uncertainties in the estimated values of f_0 and a_0 are less than 0.001 Hz and 0.02 s, respectively (see more details in Sec. III A and Sec. IV B of Ref. [49]). Hence, we do not see any evidence of a real astrophysical signal in these two outliers.

B. Veto safety

The four-step veto procedure is verified with four synthetic signals injected into 120 d of Initial LIGO S5 data recolored to Advanced LIGO O1 noise and 200 signals injected into 130 d of O1 data. The signals feature low spin wandering, drifting within one to four f_0 bins during the full observation. We do not inject signals into the sub-bands contaminated by known noise lines, so these 204 signals survive the first veto step in Sec. IV A 1 automatically. Only two out of the 204 injections are vetoed after the four steps described in Sec. IV A 1–IV A 4, yielding a false dismissal rate $< 1\%$ and demonstrating that detectable spin-wandering signals are not commonly rejected. The two vetoed injections are rejected by the $T_{\mathrm{obs}}/2$ veto. They return a slightly higher S value than $S_{\cup}$ (one in the first half, the other in the second), with $(S - S_{\cup})/S_{\cup} \leq 3\%$ and $S_{\cup} \lesssim 10$ (i.e., $< 50\%$ higher than S_{th}). In other words, the two false dismissals happen when both $(S - S_{\cup})/S_{\cup}$ and $S_{\cup}$ are small. By contrast, three out of the four candidates vetoed in Table IV (Sec. IV A 3) return $(S - S_{\cup})/S_{\cup} > 10\%$ (with $8 < S_{\cup} < 16$), and the other returns $S - S_{\cup} = 0.35$ with $S_{\cup} > 20$ (i.e., 175% higher than S_{th}). Hence, the four vetoed candidates in Table IV fail the $T_{\mathrm{obs}}/2$ veto more strongly and are unlikely to be false dismissals.

Twelve examples of the synthetic signals surviving the vetoes described in Sec. IV A 1–IV A 4 are listed in Table VII.

TABLE VII. Veto safety verification with synthetic signals. The table lists the data used for the injections (column 1), the injected signal parameters (columns 2–5), the original score $S_{\cup}$ yielded by searching the whole data set with two interferometers and $T_{\mathrm{obs}} = 10$ d (column 6), the scores from searching H1 and L1 separately (columns 7 and 8), the scores from searching the first and second half of the data separately (columns 9 and 10), and the score with $T_{\mathrm{obs}} = 20$ d (column 11). A score is marked with an asterisk if it is above threshold, but the estimated frequency differs significantly from $f_{0\mathrm{inj}}$ (i.e., wrong path returned). These twelve injections survive the four veto stages described in Sec. IV A 1–IV A 4.

Data	$f_{0\mathrm{inj}}$ (Hz)	$a_{0\mathrm{inj}}$ (s)	$h_{0\mathrm{inj}}$ (10^{-25})	$\cos\iota_{\mathrm{inj}}$	$S_{\cup}$	S_{H1}	S_{L1}	$S_{1\,\mathrm{st\ half}}$	$S_{2\,\mathrm{nd\ half}}$	$S_{20\,\mathrm{d}}$
S5	64.5774908	0.81	9.58	−0.5936	9.12097	$< S_{\mathrm{th}}$	7.42935*	$< S_{\mathrm{th}}$	7.67254	11.7985
S5	102.2907797	2.47	9.81	−0.7988	20.81940	16.17190	12.00540	20.63850	17.38740	25.81390
S5	202.8863982	2.34	11.25	−0.9205	15.80950	18.54850	17.46390	19.15680	18.9102	21.4415
S5	254.6697757	3.03	14.55	0.0375	12.50180	$< S_{\mathrm{th}}$	9.27111	10.8953	7.74954	15.0849
O1	97.2345635	2.15	4.50	0.71935	9.76216	$< S_{\mathrm{th}}$	7.53014*	7.29089	8.91108	9.98727
O1	132.1234568	0.70	4.80	−0.68154	16.86500	8.90286	8.63928	13.29010	13.30940	19.54900
O1	185.8094752	1.11	9.90	0.37952	19.05450	14.44080	12.70840	18.07160	17.95120	20.34430
O1	233.9125689	0.46	4.60	0.70917	16.71220	$< S_{\mathrm{th}}$	9.18889	12.25070	13.15180	18.02530
O1	345.3456700	1.45	7.00	0.71567	14.09400	$< S_{\mathrm{th}}$	9.15852	10.10120	12.83390	14.72410
O1	454.4563891	3.20	7.00	−0.86725	9.03162	7.54074*	$< S_{\mathrm{th}}$	$< S_{\mathrm{th}}$	$< S_{\mathrm{th}}$	9.06928
O1	525.7096896	2.81	12.90	0.66578	11.55910	7.83362	8.90156	11.35370	10.04660	13.26430
O1	635.6679700	1.98	10.00	0.72650	10.64010	$< S_{\mathrm{th}}$	$< S_{\mathrm{th}}$	8.91769	9.13239	11.56240

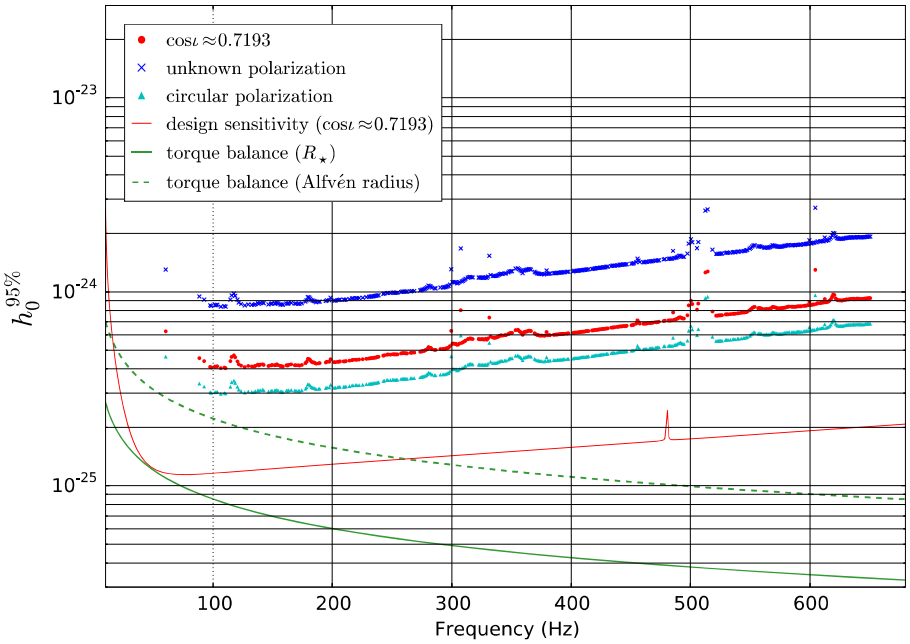

FIG. 4. Frequentist wave strain upper limits at 95% confidence ($h_0^{95\%}$) as a function of signal frequency (f_0) assuming the electromagnetically restricted orientation $\iota = 44°$ (red dots), unknown polarization with a flat prior on $\cos\iota$ (blue crosses), and circular polarization, i.e., $\cos\iota = \pm 1$ (cyan triangles). Each marker indicates the upper limit derived in the corresponding 1-Hz sub-band. Sub-bands with no marker are vetoed, e.g., contaminated by noise lines. The green solid and dashed curves indicate the theoretical torque-balance upper limits for LMXBs by taking $R_\star$ and the Alfvén radius as the accretion-torque lever arm, respectively [19]. The red curve indicates $h_0^{95\%}$ at the design sensitivity of Advanced LIGO [64], assuming $\iota = 44°$ and $T_{\rm obs} = 2$ yr.

C. Strain upper limits

In the absence of a detection, we can place an upper limit on h_0 at a desired level of confidence (usually 95%) as a function of f_0.

A Bayesian analytic approach was adopted in the previous S5 sideband search for computing the strain upper limits [34]. However, the distribution of Viterbi path probabilities is hard to calculate analytically; Viterbi paths are correlated, and the nonlinear maximization step in the algorithm is hard to handle even within the context of extreme value theory (see Sec. III C in Ref. [49]). Hence, the Bayesian approach is hard to extend to the HMM sideband search. Instead, we adopt an empirical approach to set a frequentist upper limit as follows. We define h_0^u such that the probability to detect a signal with $h_0 \geq h_0^u$ is greater than or equal to u, i.e., $\Pr(S \geq S_{\rm th} | h_0 \geq h_0^u) \geq u$. Hence, with no detection we take the $h_0^{95\%}$ value plotted in Fig. 2 (see Sec. III D) as the frequentist 95% confidence upper limit for electromagnetically restricted $\cos\iota$. It can be analytically converted to upper limits for unknown and circular polarizations using the scaling given by Eq. (8).

Figure 4 displays the upper limit derived from the O1 search combining data from H1 and L1 as a function of f_0. Each marker indicates $h_0^{95\%}$ in the corresponding 1-Hz sub-band. Bands that do not contain a marker are those containing a candidate vetoed in any of the four veto stages described in Sec. IV A 1–IV A 4. In total, 180 out of 591 1-Hz sub-bands contain vetoed candidates (see Table II). The red dots correspond to assuming $\iota = 44°$, as inferred from radio observations [59]. The blue crosses correspond to assuming unknown polarization and a flat prior on $\cos\iota$. The cyan triangles correspond to assuming circularly polarized signals (i.e., $\cos\iota = \pm 1$). At 106 Hz, the lowest 95% confidence upper limits are $h_0^{95\%} = 4.0 \times 10^{-25}$, 8.3×10^{-25}, and 3.0×10^{-25} for electromagnetically restricted $\cos\iota$, unknown polarization, and circular polarization, respectively. Hence, the electromagnetically restricted prior and circular polarization assumptions improve upon the upper limits for unknown polarization by factors of 2.08 and 2.77, respectively.

As a further check, we compare the frequentist Viterbi upper limit to the frequentist $\mathcal{C}$-statistic upper limit. We run injections in six 1-Hz sub-bands in the best 10-day stretch of the real O1 interferometer data, starting from 110 Hz, 257 Hz, 355 Hz, 454 Hz, 550 Hz, and 649 Hz, and search for them with the $\mathcal{C}$-statistic sideband pipeline [34,36]. The best 10-day data stretch is selected from O1 as follows [65,66]. A figure of merit, proportional to the signal-to-noise ratio, is defined by $\sum_{I,J}[S_h(f_I)]_J^{-1}$, where $[S_h(f_I)]_J$ is the strain noise power spectral density at discrete frequency bin f_I in the $J^{\rm th}$ SFT, and the summation is over all SFTs in each rolling 10-day stretch in O1. The 10-day data stretch with the highest value of this figure over the 60–650 Hz band is selected. We compare the values of $h_0^{95\%}$ from the

$\mathcal{C}$-statistic to the values plotted in Fig. 4. The results show that the frequentist 95% confidence upper limits from the $\mathcal{C}$-statistic are 1.46–1.74 times larger than those achieved from the search described in this paper.

V. TORQUE-BALANCE UPPER LIMIT

In LMXBs the gravitational wave strain inferred from the torque-balance scenario can be expressed as a function of the spin frequency of the neutron star $f_\star$ and the X-ray flux F_X according to [19,27,36]

$$h_0^{\rm eq} = 5.5\times10^{-27}\left(\frac{F_X}{10^{-8}\ {\rm erg\,cm^{-2}\,s^{-1}}}\right)^{1/2}\left(\frac{R_\star}{10\ {\rm km}}\right)^{3/4} \times\left(\frac{1.4\ M_\odot}{M_\star}\right)^{1/4}\left(\frac{300\ {\rm Hz}}{f_\star}\right)^{1/2}, \quad (10)$$

where $R_\star$ is the stellar radius and $M_\star$ is the stellar mass.[2] We now ask how $h_0^{\rm eq}$ compares to the results of the analysis in Sec. IV.

Let us take the electromagnetically measured $F_X = 4\times10^{-7}$ erg cm^{-2} s^{-1} [56] for Sco X-1 and the fiducial values $R_\star = 10$ km and $M_\star = 1.4\ M_\odot$. We plot $h_0^{\rm eq}$ as a function of $f_0 = 2f_\star$ in Fig. 4 (green solid curve). Near 106 Hz, where the best $h_0^{95\%}$ is reported, we obtain $h_0^{\rm eq}\approx 8.3\times10^{-26}$, which is 4.8, 10.0, and 3.6 times lower than $h_0^{95\%}$ for electromagnetically restricted $\cos\iota$, unknown polarization, and circular polarization, respectively. The design sensitivity of Advanced LIGO is expected to improve further about two-fold relative to O1 [31]. The anticipated $h_0^{95\%}$ at the design sensitivity of Advanced LIGO is plotted as a function of f_0 in Fig. 4 as the red curve, assuming an electromagnetically restricted orientation ($\iota = 44°$) and $T_{\rm obs} = 2$ yr. Near 50 Hz, $h_0^{95\%}$ reaches $h_0^{\rm eq}$.

The green solid curve in Fig. 4 is somewhat conservative [34]. If we consider the Alfvén radius to be the accretion-torque lever arm, instead of $R_\star$ as assumed in Eq. (10), then $h_0^{\rm eq}$ increases by a factor of a few. The Alfvén radius is given by [48]

$$R_A = \left(\frac{B_\star^4 R_\star^{12}}{2GM_\star\dot{M}^2}\right)^{1/7} \quad (11)$$

$$= 35\left(\frac{B_\star}{10^9\ {\rm G}}\right)^{4/7}\left(\frac{R_\star}{10\ {\rm km}}\right)^{12/7} \times\left(\frac{1.4M_\odot}{M_\star}\right)^{1/7}\left(\frac{10^{-8}M_\odot\ {\rm yr^{-1}}}{\dot{M}}\right)^{2/7}\ {\rm km}, \quad (12)$$

where $B_\star$ is the magnetic field of the star, G is Newton's gravitational constant, and $\dot{M}$ is the accretion rate. The neutron stars in LMXBs have $\dot{M}$ ranging from $\sim10^{-11}\ M_\odot{\rm yr}^{-1}$ to the Eddington limit $2\times10^{-8}\ M_\odot{\rm yr}^{-1}$ [68,69], and weak magnetic fields in the range $10^8\ {\rm G}\lesssim B_\star\lesssim 10^9$ G [19,69,70]. To estimate the maximum magnitude of the effect, we substitute $\dot{M} = 10^{-8}\ M_\odot{\rm yr}^{-1}$ and $B_\star = 10^9$ G in Eq. (12). The resulting $h_0^{\rm eq}$ is shown as the green dashed curve in Fig. 4, giving $h_0^{95\%}\approx 2h_0^{\rm eq}$ for electromagnetically restricted $\cos\iota$. At the design sensitivity of Advanced LIGO, we expect $h_0^{95\%} < h_0^{\rm eq}$ in the band 30 Hz $\lesssim f_0 \lesssim$ 250 Hz.

VI. CONCLUSION

We perform an HMM sideband search for continuous gravitational waves from Sco X-1 in Advanced LIGO O1 data from 60 Hz to 650 Hz. The analysis is computationally efficient, requiring $\lesssim 3\times10^3$ CPU-hr. We see no evidence of gravitational waves. Frequentist 95% confidence upper limits of $h_0^{95\%} = 4.0\times10^{-25}$, 8.3×10^{-25}, and 3.0×10^{-25} are derived at 106 Hz for electromagnetically restricted $\cos\iota$, unknown polarization, and circular polarization, respectively. The upper limits are derived from Monte-Carlo simulations of spin-wandering signals. They are 4.8, 10.0, and 3.6 times larger than the stellar radius torque-balance limit $h_0^{\rm eq}$, and approach $h_0^{\rm eq}$ more closely, if we treat the Alfvén radius as the accretion-torque lever arm. An analysis of two years of Advanced LIGO data at design sensitivity with this search will be able to constrain the Alfvén radius lever-arm scenario at frequencies below 300 Hz. The best existing Bayesian 90% confidence median strain upper limit from the radiometer O1 search is $h_0^{90\%} = 6.7\times10^{-25}$ at 135 Hz [45]. It converts to 95% confidence median and maximum upper limits $h_0^{95\%} = 7.8\times10^{-25}$ and $h_0^{95\%} = 1.0\times10^{-24}$, respectively, in the sub-band 134–135 Hz [44], which are comparable to the results for unknown polarization presented here.[3] Although these results are similar in sensitivity, this is the first analysis that searches over the projected semimajor axis of the binary orbit within the uncertainty of the electromagnetic measurement while taking into account the effects of spin wandering over $T_{\rm obs}$. The spin frequency of Sco X-1 has not been determined conclusively and could also lie below 60 Hz. In the future, it is hoped that the number of instrumental lines at low frequencies will be reduced, enabling analysis below 60 Hz, where $h_0^{\rm eq}$ is higher and hence easier to reach. At

[2]We assume that the system emits gravitational radiation via the mass quadrupole channel. The analogous equation for current quadrupole radiation is given in Ref. [67].

[3]The value of $h_0^{95\%}$ from the present search for unknown polarization is 6% higher and 17% lower than the median and maximum $h_0^{95\%}$ values from the radiometer search, respectively [45]. A direct comparison of the best quoted limits from the present search and the radiometer search is complicated by the different approaches of reporting upper limits. The present search returns the optimal Viterbi path (i.e., one upper limit) in each 1-Hz sub-band, while the radiometer search reports a range of upper limits.

the design sensitivity of Advanced LIGO, it is anticipated that $h_0^{95\%}$ can be improved further by a factor of two to three, reaching $h_0^{\rm eq}$ near 50 Hz. In addition to Sco X-1, the search can be applied to other X-ray binaries including Cygnus X-3, the next brightest X-ray source after Sco X-1, and sources like XTE J1751-305 and 4U 1636-536, which show periodicities in the X-ray light curves and may indicate r-mode oscillations [71–73].

ACKNOWLEDGMENTS

The authors gratefully acknowledge the support of the United States National Science Foundation (NSF) for the construction and operation of the LIGO Laboratory and Advanced LIGO as well as the Science and Technology Facilities Council (STFC) of the United Kingdom, the Max-Planck-Society (MPS), and the State of Niedersachsen/Germany for support of the construction of Advanced LIGO and construction and operation of the GEO600 detector. Additional support for Advanced LIGO was provided by the Australian Research Council. The authors gratefully acknowledge the Italian Istituto Nazionale di Fisica Nucleare (INFN), the French Centre National de la Recherche Scientifique (CNRS) and the Foundation for Fundamental Research on Matter supported by the Netherlands Organization for Scientific Research, for the construction and operation of the Virgo detector and the creation and support of the EGO consortium. The authors also gratefully acknowledge research support from these agencies as well as by the Council of Scientific and Industrial Research of India, Department of Science and Technology, India, Science & Engineering Research Board (SERB), India, Ministry of Human Resource Development, India, the Spanish Ministerio de Economía y Competitividad, the Vicepresidència i Conselleria d'Innovació, Recerca i Turisme and the Conselleria d'Educació i Universitat del Govern de les Illes Balears, the National Science Centre of Poland, the European Commission, the Royal Society, the Scottish Funding Council, the Scottish Universities Physics Alliance, the Hungarian Scientific Research Fund (OTKA), the Lyon Institute of Origins (LIO), the National Research Foundation of Korea, Industry Canada and the Province of Ontario through the Ministry of Economic Development and Innovation, the Natural Science and Engineering Research Council Canada, Canadian Institute for Advanced Research, the Brazilian Ministry of Science, Technology, and Innovation, International Center for Theoretical Physics South American Institute for Fundamental Research (ICTP-SAIFR), Russian Foundation for Basic Research, the Leverhulme Trust, the Research Corporation, Ministry of Science and Technology (MOST), Taiwan and the Kavli Foundation. The authors gratefully acknowledge the support of the NSF, STFC, MPS, INFN, CNRS and the State of Niedersachsen/Germany for provision of computational resources. This is LIGO document LIGO-P1700019.

APPENDIX A: HIDDEN MARKOV MODEL

A HMM is a finite state automaton defined by a hidden (unobservable) state variable $q(t)$ transitioning between values from the set $\{q_1, \ldots, q_{N_Q}\}$ and an observable state variable $o(t)$ taking values from the set $\{o_1, \ldots, o_{N_O}\}$ at discrete times $\{t_0, \ldots, t_{N_T}\}$. The automaton jumps between hidden states from t_n to t_{n+1} with probability

$$A_{q_j q_i} = \Pr[q(t_{n+1}) = q_j | q(t_n) = q_i] \tag{A1}$$

and is observed in the state o_j with emission probability

$$L_{o_j q_i} = \Pr[o(t_n) = o_j | q(t_n) = q_i]. \tag{A2}$$

For a Markov process, the probability that the hidden path $Q = \{q(t_0), \ldots, q(t_{N_T})\}$ gives rise to the observed sequence $O = \{o(t_0), \ldots, o(t_{N_T})\}$ is given by

$$P(Q|O) = L_{o(t_{N_T})q(t_{N_T})} A_{q(t_{N_T})q(t_{N_T-1})} \cdots L_{o(t_1)q(t_1)} \times A_{q(t_1)q(t_0)} \Pi_{q(t_0)}, \tag{A3}$$

where

$$\Pi_{q_i} = \Pr[q(t_0) = q_i] \tag{A4}$$

is the prior. The most probable path $Q^*(O) = \arg\max P(Q|O)$ maximizes $P(Q|O)$ and gives the best estimate of $q(t)$ over the total observation.

In this application, we map the discrete hidden states one-to-one to the frequency bins in the output of a frequency-domain estimator $G(f)$ (see Sec. II B) computed over an interval of length $T_{\rm drift}$, with bin size $\Delta f_{\rm drift} = 1/(2T_{\rm drift})$. We can always choose an intermediate time scale $T_{\rm drift}$ in between the duration of one SFT, $T_{\rm SFT} = 30$ min, and the total observation time $T_{\rm obs}$ in order to satisfy

$$\left| \int_t^{t+T_{\rm drift}} dt' \dot{f}_0(t') \right| < \Delta f_{\rm drift} \tag{A5}$$

for all t.[4] We assume that the spin wandering caused by accretion noise in Sco X-1 follows an unbiased Wiener process, in which $f_0(t)$ experiences a random walk and stays within $\Delta f_{\rm drift}$ for a duration less than a conservatively chosen $T_{\rm drift} = 10$ d, based on the assumption that the deviation of the accretion torque from its average value flips sign on the time scale of observed fluctuations in the

[4]Frequency-domain, continuous-wave LIGO searches operate on SFTs rather than the time series of the detector output [1].

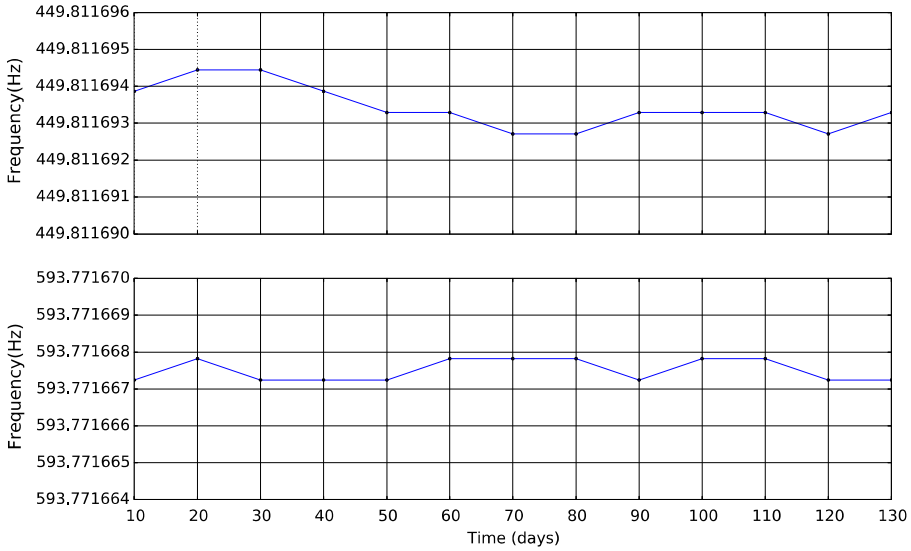

FIG. 5. Optimal Viterbi paths for the two survivors from Sec. IV A 3.

X-ray flux [34,74].[5] Assuming continuous frequency wandering (i.e., no neutron star rotational glitches), Eq. (A1) simplifies to the tridiagonal form

$$A_{q_{i+1}q_i} = A_{q_iq_i} = A_{q_{i-1}q_i} = \frac{1}{3}, \tag{A6}$$

with all other entries vanishing. The emission probability can be expressed in terms of $G(f)$ as

$$L_{o(t)q_i} \propto \exp[G(f_{0i})], \tag{A7}$$

where $G(f_{0i})$ is the log likelihood that the gravitational-wave signal frequency f_0 (e.g., twice the spin frequency of the star) lies in the frequency bin $[f_{0i}, f_{0i} + \Delta f_{\mathrm{drift}}]$ during the interval $[t, t + T_{\mathrm{drift}}]$. As we have no advance knowledge of f_0, we choose a uniform prior, viz.

$$\Pi_{q_i} = N_Q^{-1}. \tag{A8}$$

APPENDIX B: VITERBI ALGORITHM

The classic Viterbi algorithm [51] provides a recursive, computationally efficient route to computing $Q^*(O)$, reducing the number of operations to $(N_T + 1)N_Q \ln N_Q$ by binary maximization [50]. At every forward step k ($1 \le k \le N_T$) in the recursion, the algorithm eliminates all but N_Q possible state sequences, and stores the N_Q maximum probabilities ($1 \le i \le N_Q$)

$$\delta_{q_i}(t_k) = L_{o(t_k)q_i} \max_{1\le j\le N_Q} [A_{q_iq_j}\delta_{q_j}(t_{k-1})]. \tag{B1}$$

It also stores the previous-step states of origin,

$$\Phi_{q_i}(t_k) = \arg\max_{1\le j\le N_Q} [A_{q_iq_j}\delta_{q_j}(t_{k-1})], \tag{B2}$$

that maximize the probability at that step. The optimal Viterbi path is then reconstructed by backtracking according to

$$q^*(t_k) = \Phi_{q^*(t_{k+1})}(t_{k+1}) \tag{B3}$$

for $0 \le k \le N_T - 1$. A detailed description of the algorithm can be found in Sec. II D of Ref. [49].

APPENDIX C: $T_{\mathrm{obs}}/2$ VETO SURVIVORS: OPTIMAL VITERBI PATHS

In the T_{drift} veto described in Sec. IV A 4, we categorize the two survivors according to their optimal paths detected in the original search. The optimal paths of the two survivors are plotted in Fig. 5, showing the estimated frequency f_0 as a function of time evaluated at the endpoint of each Viterbi step. The paths near 449 Hz and 593 Hz drift within three and one f_0 bins, respectively, over T_{obs}. They display low spin wandering.

[5]For constant spin up or spin down, we are able to track a maximum rate $|\dot{f}_0| = \Delta f_{\mathrm{drift}} T_{\mathrm{drift}}^{-1} = 7 \times 10^{-13}$ Hz s^{-1}. By way of comparison, without considering accretion noise, the secular spin-down (or spin-up) rate of LMXBs satisfies $|\dot{f}_0| \lesssim 10^{-14}$ Hz s^{-1} [70].

[1] K. Riles, Prog. Part. Nucl. Phys. **68**, 1 (2013).
[2] G. M. Harry *et al.*, Classical Quantum Gravity **27**, 084006 (2010).
[3] J. Aasi *et al.* (The LIGO Scientific Collaboration), Classical Quantum Gravity **32**, 074001 (2015).
[4] F. Acernese *et al.*, Classical Quantum Gravity **32**, 024001 (2015).
[5] N. Andersson, V. Ferrari, D. I. Jones, K. D. Kokkotas, B. Krishnan, J. S. Read, L. Rezzolla, and B. Zink, Gen. Relativ. Gravit. **43**, 409 (2011).
[6] G. Ushomirsky, C. Cutler, and L. Bildsten, Mon. Not. R. Astron. Soc. **319**, 902 (2000).
[7] N. K. Johnson-McDaniel and B. J. Owen, Phys. Rev. D **88**, 044004 (2013).
[8] C. Cutler, Phys. Rev. D **66**, 084025 (2002).
[9] A. Mastrano, A. Melatos, A. Reisenegger, and T. Akgün, Mon. Not. R. Astron. Soc. **417**, 2288 (2011).
[10] P. D. Lasky and A. Melatos, Phys. Rev. D **88**, 103005 (2013).
[11] B. J. Owen, L. Lindblom, C. Cutler, B. F. Schutz, A. Vecchio, and N. Andersson, Phys. Rev. D **58**, 084020 (1998).
[12] J. S. Heyl, Astrophys. J. **574**, L57 (2002).
[13] P. Arras, E. E. Flanagan, S. M. Morsink, A. K. Schenk, S. A. Teukolsky, and I. Wasserman, Astrophys. J. **591**, 1129 (2003).
[14] R. Bondarescu, S. A. Teukolsky, and I. Wasserman, Phys. Rev. D **79**, 104003 (2009).
[15] C. Peralta, A. Melatos, M. Giacobello, and A. Ooi, Astrophys. J. **644**, L53 (2006).
[16] C. A. van Eysden and A. Melatos, Classical Quantum Gravity **25**, 225020 (2008).
[17] M. F. Bennett, C. A. Van Eysden, and A. Melatos, Mon. Not. R. Astron. Soc. **409**, 1705 (2010).
[18] A. Melatos, J. A. Douglass, and T. P. Simula, Astrophys. J. **807**, 132 (2015).
[19] L. Bildsten, Astrophys. J. Lett. **501**, L89 (1998).
[20] N. Andersson, K. D. Kokkotas, and N. Stergioulas, Astrophys. J. **516**, 307 (1999).
[21] M. Nayyar and B. J. Owen, Phys. Rev. D **73**, 084001 (2006).
[22] A. Melatos, Adv. Space Res. **40**, 1472 (2007).
[23] M. Vigelius and A. Melatos, Mon. Not. R. Astron. Soc. **395**, 1972 (2009).
[24] D. Chakrabarty, E. H. Morgan, M. P. Muno, D. K. Galloway, R. Wijnands, M. van der Klis, and C. B. Markwardt, Nature (London) **424**, 42 (2003).
[25] G. B. Cook, S. L. Shapiro, and S. A. Teukolsky, Astrophys. J. **424**, 823 (1994).
[26] J. Papaloizou and J. E. Pringle, Mon. Not. R. Astron. Soc. **184**, 501 (1978).
[27] R. V. Wagoner, Astrophys. J. **278**, 345 (1984).
[28] B. Abbott *et al.* (LIGO Scientific Collaboration), Rep. Prog. Phys. **72**, 076901 (2009).
[29] J. Aasi *et al.* (The LIGO Scientific Collaboration and The Virgo Collaboration), arXiv:1203.2674.
[30] G. M. Harry (The LIGO Scientific Collaboration), Classical Quantum Gravity **27**, 084006 (2010).
[31] B. Abbott *et al.*, Phys. Rev. Lett. **116**, 131103 (2016).
[32] P. Jaranowski, A. Królak, and B. F. Schutz, Phys. Rev. D **58**, 063001 (1998).
[33] B. Abbott *et al.*, Phys. Rev. D **76**, 082001 (2007).
[34] J. Aasi *et al.*, Phys. Rev. D **91**, 062008 (2015).
[35] C. Messenger and G. Woan, Classical Quantum Gravity **24**, S469 (2007).
[36] L. Sammut, C. Messenger, A. Melatos, and B. J. Owen, Phys. Rev. D **89**, 043001 (2014).
[37] E. Goetz and K. Riles, Classical Quantum Gravity **28**, 215006 (2011).
[38] J. Aasi *et al.*, Phys. Rev. D **90**, 062010 (2014).
[39] G. D. Meadors, E. Goetz, and K. Riles, Classical Quantum Gravity **33**, 105017 (2016).
[40] G. D. Meadors, E. Goetz, K. Riles, T. Creighton, and F. Robinet, Phys. Rev. D **95**, 042005 (2017).
[41] S. W. Ballmer, Classical Quantum Gravity **23**, S179 (2006).
[42] B. Abbott *et al.*, Phys. Rev. D **76**, 082003 (2007).
[43] J. Abadie *et al.*, Phys. Rev. Lett. **107**, 271102 (2011).
[44] C. Messenger, LIGO Report No. T1000195, 2011.
[45] B. Abbott *et al.*, Phys. Rev. Lett. **118**, 121102 (2017).
[46] M. deKool and U. Anzer, Mon. Not. R. Astron. Soc. **262**, 726 (1993).
[47] A. Baykal and H. Oegelman, Astron. Astrophys. **267**, 119 (1993).
[48] L. Bildsten, D. Chakrabarty, J. Chiu, M. H. Finger, D. T. Koh, R. W. Nelson, T. A. Prince, B. C. Rubin, D. M. Scott, M. Stollberg, B. A. Vaughan, C. A. Wilson, and R. B. Wilson, Astrophys. J. Suppl. Ser. **113**, 367 (1997).
[49] S. Suvorova, L. Sun, A. Melatos, W. Moran, and R. J. Evans, Phys. Rev. D **93**, 123009 (2016).
[50] B. G. Quinn and E. J. Hannan, *The Estimation and Tracking of Frequency* (Cambridge University Press, Cambridge, England, 2001), p. 266.
[51] A. Viterbi, IEEE Trans. Inf. Theory **13**, 260 (1967).
[52] S. M. Ransom, J. M. Cordes, and S. S. Eikenberry, Astrophys. J. **589**, 911 (2003).
[53] M. Abramowitz and I. A. Stegun, *Handbook of Mathematical Functions: With Formulas, Graphs, and Mathematical Tables*, *National Bureau of Standards Applied Mathematics Series* Vol. 55 (U. S. Government Printing Office, Washington, D. C, 1964).
[54] R. Prix, LIGO Report No. T0900149, 2011.
[55] C. F. Bradshaw, E. B. Fomalont, and B. J. Geldzahler, Astrophys. J. **512**, L121 (1999).
[56] A. L. Watts, B. Krishnan, L. Bildsten, and B. F. Schutz, Mon. Not. R. Astron. Soc. **389**, 839 (2008).
[57] D. K. Galloway, S. Premachandra, D. Steeghs, T. Marsh, J. Casares, and R. Cornelisse, Astrophys. J. **781**, 14 (2014).
[58] D. Steeghs, and J. Casares, Astrophys. J. **568**, 273 (2002).
[59] E. B. Fomalont, B. J. Geldzahler, and C. F. Bradshaw, Astrophys. J. **558**, 283 (2001).
[60] Z. Wang, Ph.D. thesis, Warwick University, 2017.
[61] Z. Wang *et al.* (private communication).
[62] C. Messenger, H. J. Bulten, S. G. Crowder, V. Dergachev, D. K. Galloway, E. Goetz, R. J. G. Jonker, P. D. Lasky, G. D. Meadors, A. Melatos, S. Premachandra, K. Riles, L. Sammut, E. H. Thrane, J. T. Whelan, and Y. Zhang, Phys. Rev. D **92**, 023006 (2015).
[63] J. T. Whelan, S. Sundaresan, Y. Zhang, and P. Peiris, Phys. Rev. D **91**, 102005 (2015).

[64] D. H. Shoemaker *et al.* (The LIGO Scientific Collaboration), LIGO Report No. T0900288, 2009, https://dcc.ligo.org/LIGO-T0900288/public.
[65] K. W. Wette, Ph.D. thesis, The Australian National University, 2009.
[66] J. Abadie *et al.*, Astrophys. J. **722**, 1504 (2010).
[67] B. J. Owen, Phys. Rev. D **82**, 104002 (2010).
[68] H. Ritter and U. Kolb, Astron. Astrophys. **404**, 301 (2003).
[69] L. Sammut, Ph.D. thesis, The University of Melbourne, 2015.
[70] A. Patruno and A. L. Watts, arXiv:1206.2727.
[71] L. Cadonati *et al.* (The LIGO Scientific Collaboration and The Virgo Collaboration), LIGO Report No. T1600115, 2016, https://dcc.ligo.org/LIGO-T1600115/public.
[72] S. Mahmoodifar and T. Strohmayer, Astrophys. J. **773**, 140 (2013).
[73] B. Haskell, Int. J. Mod. Phys. E **24**, 1541007 (2015).
[74] G. Ushomirsky, L. Bildsten, and C. Cutler, arXiv:0001129.

B. P. Abbott,[1] R. Abbott,[1] T. D. Abbott,[2] F. Acernese,[3,4] K. Ackley,[5] C. Adams,[6] T. Adams,[7] P. Addesso,[8] R. X. Adhikari,[1] V. B. Adya,[9] C. Affeldt,[9] M. Afrough,[10] B. Agarwal,[11] K. Agatsuma,[12] N. Aggarwal,[13] O. D. Aguiar,[14] L. Aiello,[15,16] A. Ain,[17] P. Ajith,[18] B. Allen,[9,19,20] G. Allen,[11] A. Allocca,[21,22] H. Almoubayyed,[23] P. A. Altin,[24] A. Amato,[25] A. Ananyeva,[1] S. B. Anderson,[1] W. G. Anderson,[19] S. Antier,[26] S. Appert,[1] K. Arai,[1] M. C. Araya,[1] J. S. Areeda,[27] N. Arnaud,[26,28] K. G. Arun,[29] S. Ascenzi,[30,16] G. Ashton,[9] M. Ast,[31] S. M. Aston,[6] P. Astone,[32] P. Aufmuth,[20] C. Aulbert,[9] K. AultONeal,[33] A. Avila-Alvarez,[27] S. Babak,[34] P. Bacon,[35] M. K. M. Bader,[12] S. Bae,[36] P. T. Baker,[37,38] F. Baldaccini,[39,40] G. Ballardin,[28] S. W. Ballmer,[41] S. Banagiri,[42] J. C. Barayoga,[1] S. E. Barclay,[23] B. C. Barish,[1] D. Barker,[43] F. Barone,[3,4] B. Barr,[23] L. Barsotti,[13] M. Barsuglia,[35] D. Barta,[44] J. Bartlett,[43] I. Bartos,[45] R. Bassiri,[46] A. Basti,[21,22] J. C. Batch,[43] C. Baune,[9] M. Bawaj,[47,40] M. Bazzan,[48,49] B. Bécsy,[50] C. Beer,[9] M. Bejger,[51] I. Belahcene,[26] A. S. Bell,[23] B. K. Berger,[1] G. Bergmann,[9] C. P. L. Berry,[52] D. Bersanetti,[53,54] A. Bertolini,[12] Z. B. Etienne,[37,38] J. Betzwieser,[6] S. Bhagwat,[41] R. Bhandare,[55] I. A. Bilenko,[56] G. Billingsley,[1] C. R. Billman,[5] J. Birch,[6] R. Birney,[57] O. Birnholtz,[9] S. Biscans,[13] A. Bisht,[20] M. Bitossi,[28,22] C. Biwer,[41] M. A. Bizouard,[26] J. K. Blackburn,[1] J. Blackman,[58] C. D. Blair,[59] D. G. Blair,[59] R. M. Blair,[43] S. Bloemen,[60] O. Bock,[9] N. Bode,[9] M. Boer,[61] G. Bogaert,[61] A. Bohe,[34] F. Bondu,[62] R. Bonnand,[7] B. A. Boom,[12] R. Bork,[1] V. Boschi,[21,22] S. Bose,[63,17] Y. Bouffanais,[35] A. Bozzi,[28] C. Bradaschia,[22] P. R. Brady,[19] V. B. Braginsky,[56,†] M. Branchesi,[64,65] J. E. Brau,[66] T. Briant,[67] A. Brillet,[61] M. Brinkmann,[9] V. Brisson,[26] P. Brockill,[19] J. E. Broida,[68] A. F. Brooks,[1] D. A. Brown,[41] D. D. Brown,[52] N. M. Brown,[13] S. Brunett,[1] C. C. Buchanan,[2] A. Buikema,[13] T. Bulik,[69] H. J. Bulten,[70,12] A. Buonanno,[34,71] D. Buskulic,[7] C. Buy,[35] R. L. Byer,[46] M. Cabero,[9] L. Cadonati,[72] G. Cagnoli,[25,73] C. Cahillane,[1] J. Calderón Bustillo,[72] T. A. Callister,[1] E. Calloni,[74,4] J. B. Camp,[75] M. Canepa,[53,54] P. Canizares,[60] K. C. Cannon,[76] H. Cao,[77] J. Cao,[78] C. D. Capano,[9] E. Capocasa,[35] F. Carbognani,[28] S. Caride,[79] M. F. Carney,[80] J. Casanueva Diaz,[26] C. Casentini,[30,16] S. Caudill,[19] M. Cavaglià,[10] F. Cavalier,[26] R. Cavalieri,[28] G. Cella,[22] C. B. Cepeda,[1] L. Cerboni Baiardi,[64,65] G. Cerretani,[21,22] E. Cesarini,[30,16] S. J. Chamberlin,[81] M. Chan,[23] S. Chao,[82] P. Charlton,[83] E. Chassande-Mottin,[35] D. Chatterjee,[19] B. D. Cheeseboro,[37,38] H. Y. Chen,[84] Y. Chen,[58] H.-P. Cheng,[5] A. Chincarini,[54] A. Chiummo,[28] T. Chmiel,[80] H. S. Cho,[85] M. Cho,[71] J. H. Chow,[24] N. Christensen,[68,61] Q. Chu,[59] A. J. K. Chua,[86] S. Chua,[67] A. K. W. Chung,[87] S. Chung,[59] G. Ciani,[5] R. Ciolfi,[88,89] C. E. Cirelli,[46] A. Cirone,[53,54] F. Clara,[43] J. A. Clark,[72] F. Cleva,[61] C. Cocchieri,[10] E. Coccia,[15,16] P.-F. Cohadon,[67] A. Colla,[90,32] C. G. Collette,[91] L. R. Cominsky,[92] M. Constancio Jr.,[14] L. Conti,[49] S. J. Cooper,[52] P. Corban,[6] T. R. Corbitt,[2] K. R. Corley,[45] N. Cornish,[93] A. Corsi,[79] S. Cortese,[28] C. A. Costa,[14] M. W. Coughlin,[68] S. B. Coughlin,[94,95] J.-P. Coulon,[61] S. T. Countryman,[45] P. Couvares,[1] P. B. Covas,[96] E. E. Cowan,[72] D. M. Coward,[59] M. J. Cowart,[6] D. C. Coyne,[1] R. Coyne,[79] J. D. E. Creighton,[19] T. D. Creighton,[97] J. Cripe,[2] S. G. Crowder,[98] T. J. Cullen,[27] A. Cumming,[23] L. Cunningham,[23] E. Cuoco,[28] T. Dal Canton,[75] S. L. Danilishin,[20,9] S. D'Antonio,[16] K. Danzmann,[20,9] A. Dasgupta,[99] C. F. Da Silva Costa,[5] V. Dattilo,[28] I. Dave,[55] M. Davier,[26] G. S. Davies,[23] D. Davis,[41] E. J. Daw,[100] B. Day,[72] S. De,[41] D. DeBra,[46] E. Deelman,[101] J. Degallaix,[25] M. De Laurentis,[74,4] S. Deléglise,[67] W. Del Pozzo,[52,21,22] T. Denker,[9] T. Dent,[9] V. Dergachev,[34] R. De Rosa,[74,4] R. T. DeRosa,[6] R. DeSalvo,[102] J. Devenson,[57] R. C. Devine,[37,38] S. Dhurandhar,[17] M. C. Díaz,[97] L. Di Fiore,[4] M. Di Giovanni,[103,89] T. Di Girolamo,[74,4,45] A. Di Lieto,[21,22] S. Di Pace,[90,32] I. Di Palma,[90,32] F. Di Renzo,[21,22] Z. Doctor,[84] V. Dolique,[25] F. Donovan,[13] K. L. Dooley,[10] S. Doravari,[9] I. Dorrington,[95] R. Douglas,[23] M. Dovale Álvarez,[52] T. P. Downes,[19] M. Drago,[9] R. W. P. Drever,[1,†] J. C. Driggers,[43] Z. Du,[78] M. Ducrot,[7] J. Duncan,[94] S. E. Dwyer,[43] T. B. Edo,[100] M. C. Edwards,[68] A. Effler,[6] H.-B. Eggenstein,[9] P. Ehrens,[1] J. Eichholz,[1] S. S. Eikenberry,[5] R. C. Essick,[13] T. Etzel,[1] M. Evans,[13] T. M. Evans,[6] M. Factourovich,[45] V. Fafone,[30,16,15] H. Fair,[41] S. Fairhurst,[95] X. Fan,[78] S. Farinon,[54] B. Farr,[84] W. M. Farr,[52] E. J. Fauchon-Jones,[95] M. Favata,[104] M. Fays,[95]

H. Fehrmann,[9] J. Feicht,[1] M. M. Fejer,[46] A. Fernandez-Galiana,[13] I. Ferrante,[21,22] E. C. Ferreira,[14] F. Ferrini,[28] F. Fidecaro,[21,22] I. Fiori,[28] D. Fiorucci,[35] R. P. Fisher,[41] R. Flaminio,[25,105] M. Fletcher,[23] H. Fong,[106] P. W. F. Forsyth,[24] S. S. Forsyth,[72] J.-D. Fournier,[61] S. Frasca,[90,32] F. Frasconi,[22] Z. Frei,[50] A. Freise,[52] R. Frey,[66] V. Frey,[26] E. M. Fries,[1] P. Fritschel,[13] V. V. Frolov,[6] P. Fulda,[5,75] M. Fyffe,[6] H. Gabbard,[9] M. Gabel,[107] B. U. Gadre,[17] S. M. Gaebel,[52] J. R. Gair,[108] L. Gammaitoni,[39] M. R. Ganija,[77] S. G. Gaonkar,[17] F. Garufi,[74,4] S. Gaudio,[33] G. Gaur,[109] V. Gayathri,[110] N. Gehrels,[75,†] G. Gemme,[54] E. Genin,[28] A. Gennai,[22] D. George,[11] J. George,[55] L. Gergely,[111] V. Germain,[7] S. Ghonge,[72] Abhirup Ghosh,[18] Archisman Ghosh,[18,12] S. Ghosh,[60,12] J. A. Giaime,[2,6] K. D. Giardina,[6] A. Giazotto,[22] K. Gill,[33] L. Glover,[102] E. Goetz,[9] R. Goetz,[5] S. Gomes,[95] G. González,[2] J. M. Gonzalez Castro,[21,22] A. Gopakumar,[112] M. L. Gorodetsky,[56] S. E. Gossan,[1] M. Gosselin,[28] R. Gouaty,[7] A. Grado,[113,4] C. Graef,[23] M. Granata,[25] A. Grant,[23] S. Gras,[13] C. Gray,[43] G. Greco,[64,65] A. C. Green,[52] P. Groot,[60] H. Grote,[9] S. Grunewald,[34] P. Gruning,[26] G. M. Guidi,[64,65] X. Guo,[78] A. Gupta,[81] M. K. Gupta,[99] K. E. Gushwa,[1] E. K. Gustafson,[1] R. Gustafson,[114] B. R. Hall,[63] E. D. Hall,[1] G. Hammond,[23] M. Haney,[112] M. M. Hanke,[9] J. Hanks,[43] C. Hanna,[81] O. A. Hannuksela,[87] J. Hanson,[6] T. Hardwick,[2] J. Harms,[64,65] G. M. Harry,[115] I. W. Harry,[34] M. J. Hart,[23] C.-J. Haster,[106] K. Haughian,[23] J. Healy,[116] A. Heidmann,[67] M. C. Heintze,[6] H. Heitmann,[61] P. Hello,[26] G. Hemming,[28] M. Hendry,[23] I. S. Heng,[23] J. Hennig,[23] J. Henry,[116] A. W. Heptonstall,[1] M. Heurs,[9,20] S. Hild,[23] D. Hoak,[28] D. Hofman,[25] K. Holt,[6] D. E. Holz,[84] P. Hopkins,[95] C. Horst,[19] J. Hough,[23] E. A. Houston,[23] E. J. Howell,[59] Y. M. Hu,[9] E. A. Huerta,[11] D. Huet,[26] B. Hughey,[33] S. Husa,[96] S. H. Huttner,[23] T. Huynh-Dinh,[6] N. Indik,[9] D. R. Ingram,[43] R. Inta,[79] G. Intini,[90,32] H. N. Isa,[23] J.-M. Isac,[67] M. Isi,[1] B. R. Iyer,[18] K. Izumi,[43] T. Jacqmin,[67] K. Jani,[72] P. Jaranowski,[117] S. Jawahar,[118] F. Jiménez-Forteza,[96] W. W. Johnson,[2] D. I. Jones,[119] R. Jones,[23] R. J. G. Jonker,[12] L. Ju,[59] J. Junker,[9] C. V. Kalaghatgi,[95] V. Kalogera,[94] S. Kandhasamy,[6] G. Kang,[36] J. B. Kanner,[1] S. Karki,[66] K. S. Karvinen,[9] M. Kasprzack,[2] M. Katolik,[11] E. Katsavounidis,[13] W. Katzman,[6] S. Kaufer,[20] K. Kawabe,[43] F. Kéfélian,[61] D. Keitel,[23] A. J. Kemball,[11] R. Kennedy,[100] C. Kent,[95] J. S. Key,[120] F. Y. Khalili,[56] I. Khan,[15,16] S. Khan,[9] Z. Khan,[99] E. A. Khazanov,[121] N. Kijbunchoo,[43] Chunglee Kim,[122] J. C. Kim,[123] W. Kim,[77] W. S. Kim,[124] Y.-M. Kim,[85,122] S. J. Kimbrell,[72] E. J. King,[77] P. J. King,[43] R. Kirchhoff,[9] J. S. Kissel,[43] L. Kleybolte,[31] S. Klimenko,[5] P. Koch,[9] S. M. Koehlenbeck,[9] S. Koley,[12] V. Kondrashov,[1] A. Kontos,[13] M. Korobko,[31] W. Z. Korth,[1] I. Kowalska,[69] D. B. Kozak,[1] C. Krämer,[9] V. Kringel,[9] B. Krishnan,[9] A. Królak,[125,126] G. Kuehn,[9] P. Kumar,[106] R. Kumar,[99] S. Kumar,[18] L. Kuo,[82] A. Kutynia,[125] S. Kwang,[19] B. D. Lackey,[34] K. H. Lai,[87] M. Landry,[43] R. N. Lang,[19] J. Lange,[116] B. Lantz,[46] R. K. Lanza,[13] A. Lartaux-Vollard,[26] P. D. Lasky,[127] M. Laxen,[6] A. Lazzarini,[1] C. Lazzaro,[49] P. Leaci,[90,32] S. Leavey,[23] C. H. Lee,[85] H. K. Lee,[128] H. M. Lee,[122] H. W. Lee,[123] K. Lee,[23] J. Lehmann,[9] A. Lenon,[37,38] M. Leonardi,[103,89] N. Leroy,[26] N. Letendre,[7] Y. Levin,[127] T. G. F. Li,[87] A. Libson,[13] T. B. Littenberg,[129] J. Liu,[59] N. A. Lockerbie,[118] L. T. London,[95] J. E. Lord,[41] M. Lorenzini,[15,16] V. Loriette,[130] M. Lormand,[6] G. Losurdo,[22] J. D. Lough,[9,20] G. Lovelace,[27] H. Lück,[20,9] D. Lumaca,[30,16] A. P. Lundgren,[9] R. Lynch,[13] Y. Ma,[58] S. Macfoy,[57] B. Machenschalk,[9] M. MacInnis,[13] D. M. Macleod,[2] I. Magaña Hernandez,[87] F. Magaña-Sandoval,[41] L. Magaña Zertuche,[41] R. M. Magee,[81] E. Majorana,[32] I. Maksimovic,[130] N. Man,[61] V. Mandic,[42] V. Mangano,[23] G. L. Mansell,[24] M. Manske,[19] M. Mantovani,[28] F. Marchesoni,[47,40] F. Marion,[7] S. Márka,[45] Z. Márka,[45] C. Markakis,[11] A. S. Markosyan,[46] E. Maros,[1] F. Martelli,[64,65] L. Martellini,[61] I. W. Martin,[23] D. V. Martynov,[13] J. N. Marx,[1] K. Mason,[13] A. Masserot,[7] T. J. Massinger,[1] M. Masso-Reid,[23] S. Mastrogiovanni,[90,32] A. Matas,[42] F. Matichard,[13] L. Matone,[45] N. Mavalvala,[13] R. Mayani,[101] N. Mazumder,[63] R. McCarthy,[43] D. E. McClelland,[24] S. McCormick,[6] L. McCuller,[13] S. C. McGuire,[131] G. McIntyre,[1] J. McIver,[1] D. J. McManus,[24] T. McRae,[24] S. T. McWilliams,[37,38] D. Meacher,[81] G. D. Meadors,[34,9] J. Meidam,[12] E. Mejuto-Villa,[8] A. Melatos,[132] G. Mendell,[43] R. A. Mercer,[19] E. L. Merilh,[43] M. Merzougui,[61] S. Meshkov,[1] C. Messenger,[23] C. Messick,[81] R. Metzdorff,[67] P. M. Meyers,[42] F. Mezzani,[32,90] H. Miao,[52] C. Michel,[25] H. Middleton,[52] E. E. Mikhailov,[133] L. Milano,[74,4] A. L. Miller,[5] A. Miller,[90,32] B. B. Miller,[94] J. Miller,[13] M. Millhouse,[93] O. Minazzoli,[61] Y. Minenkov,[16] J. Ming,[34] C. Mishra,[134] S. Mitra,[17] V. P. Mitrofanov,[56] G. Mitselmakher,[5] R. Mittleman,[13] A. Moggi,[22] M. Mohan,[28] S. R. P. Mohapatra,[13] M. Montani,[64,65] B. C. Moore,[104] C. J. Moore,[86] D. Moraru,[43] G. Moreno,[43] S. R. Morriss,[97] B. Mours,[7] C. M. Mow-Lowry,[52] G. Mueller,[5] A. W. Muir,[95] Arunava Mukherjee,[9] D. Mukherjee,[19] S. Mukherjee,[97] N. Mukund,[17] A. Mullavey,[6] J. Munch,[77] E. A. M. Muniz,[41] P. G. Murray,[23] K. Napier,[72] I. Nardecchia,[30,16] L. Naticchioni,[90,32] R. K. Nayak,[135] G. Nelemans,[60,12] T. J. N. Nelson,[6] M. Neri,[53,54] M. Nery,[9] A. Neunzert,[114] J. M. Newport,[115] G. Newton,[23,†] K. K. Y. Ng,[87] T. T. Nguyen,[24] D. Nichols,[60] A. B. Nielsen,[9] S. Nissanke,[60,12] A. Nitz,[9] A. Noack,[9] F. Nocera,[28] D. Nolting,[6] M. E. N. Normandin,[97] L. K. Nuttall,[41] J. Oberling,[43] E. Ochsner,[19] E. Oelker,[13] G. H. Ogin,[107] J. J. Oh,[124] S. H. Oh,[124] F. Ohme,[9] M. Oliver,[96] P. Oppermann,[9] Richard J. Oram,[6] B. O'Reilly,[6] R. Ormiston,[42] L. F. Ortega,[5] R. O'Shaughnessy,[116] D. J. Ottaway,[77]

H. Overmier,[6] B. J. Owen,[79] A. E. Pace,[81] J. Page,[129] M. A. Page,[59] A. Pai,[110] S. A. Pai,[55] J. R. Palamos,[66] O. Palashov,[121] C. Palomba,[32] A. Pal-Singh,[31] H. Pan,[82] B. Pang,[58] P. T. H. Pang,[87] C. Pankow,[94] F. Pannarale,[95] B. C. Pant,[55] F. Paoletti,[22] A. Paoli,[28] M. A. Papa,[34,19,9] H. R. Paris,[46] W. Parker,[6] D. Pascucci,[23] A. Pasqualetti,[28] R. Passaquieti,[21,22] D. Passuello,[22] B. Patricelli,[136,22] B. L. Pearlstone,[23] M. Pedraza,[1] R. Pedurand,[25,137] L. Pekowsky,[41] A. Pele,[6] S. Penn,[138] C. J. Perez,[43] A. Perreca,[1,103,89] L. M. Perri,[94] H. P. Pfeiffer,[106] M. Phelps,[23] O. J. Piccinni,[90,32] M. Pichot,[61] F. Piergiovanni,[64,65] V. Pierro,[8] G. Pillant,[28] L. Pinard,[25] I. M. Pinto,[8] M. Pitkin,[23] R. Poggiani,[21,22] P. Popolizio,[28] E. K. Porter,[35] A. Post,[9] J. Powell,[23] J. Prasad,[17] J. W. W. Pratt,[33] V. Predoi,[95] T. Prestegard,[19] M. Prijatelj,[9] M. Principe,[8] S. Privitera,[34] R. Prix,[9] G. A. Prodi,[103,89] L. G. Prokhorov,[56] O. Puncken,[9] M. Punturo,[40] P. Puppo,[32] M. Pürrer,[34] H. Qi,[19] J. Qin,[59] S. Qiu,[127] V. Quetschke,[97] E. A. Quintero,[1] R. Quitzow-James,[66] F. J. Raab,[43] D. S. Rabeling,[24] H. Radkins,[43] P. Raffai,[50] S. Raja,[55] C. Rajan,[55] M. Rakhmanov,[97] K. E. Ramirez,[97] P. Rapagnani,[90,32] V. Raymond,[34] M. Razzano,[21,22] J. Read,[27] T. Regimbau,[61] L. Rei,[54] S. Reid,[57] D. H. Reitze,[1,5] H. Rew,[133] S. D. Reyes,[41] F. Ricci,[90,32] P. M. Ricker,[11] S. Rieger,[9] K. Riles,[114] M. Rizzo,[116] N. A. Robertson,[1,23] R. Robie,[23] F. Robinet,[26] A. Rocchi,[16] L. Rolland,[7] J. G. Rollins,[1] V. J. Roma,[66] R. Romano,[3,4] C. L. Romel,[43] J. H. Romie,[6] D. Rosińska,[139,51] M. P. Ross,[140] S. Rowan,[23] A. Rüdiger,[9] P. Ruggi,[28] K. Ryan,[43] M. Rynge,[101] S. Sachdev,[1] T. Sadecki,[43] L. Sadeghian,[19] M. Sakellariadou,[141] L. Salconi,[28] M. Saleem,[110] F. Salemi,[9] A. Samajdar,[135] L. Sammut,[127] L. M. Sampson,[94] E. J. Sanchez,[1] V. Sandberg,[43] B. Sandeen,[94] J. R. Sanders,[41] B. Sassolas,[25] B. S. Sathyaprakash,[81,95] P. R. Saulson,[41] O. Sauter,[114] R. L. Savage,[43] A. Sawadsky,[20] P. Schale,[66] J. Scheuer,[94] E. Schmidt,[33] J. Schmidt,[9] P. Schmidt,[1,60] R. Schnabel,[31] R. M. S. Schofield,[66] A. Schönbeck,[31] E. Schreiber,[9] D. Schuette,[9,20] B. W. Schulte,[9] B. F. Schutz,[95,9] S. G. Schwalbe,[33] J. Scott,[23] S. M. Scott,[24] E. Seidel,[11] D. Sellers,[6] A. S. Sengupta,[142] D. Sentenac,[28] V. Sequino,[30,16] A. Sergeev,[121] D. A. Shaddock,[24] T. J. Shaffer,[43] A. A. Shah,[129] M. S. Shahriar,[94] L. Shao,[34] B. Shapiro,[46] P. Shawhan,[71] A. Sheperd,[19] D. H. Shoemaker,[13] D. M. Shoemaker,[72] K. Siellez,[72] X. Siemens,[19] M. Sieniawska,[51] D. Sigg,[43] A. D. Silva,[14] A. Singer,[1] L. P. Singer,[75] A. Singh,[34,9,20] R. Singh,[2] A. Singhal,[15,32] A. M. Sintes,[96] B. J. J. Slagmolen,[24] B. Smith,[6] J. R. Smith,[27] R. J. E. Smith,[1] E. J. Son,[124] J. A. Sonnenberg,[19] B. Sorazu,[23] F. Sorrentino,[54] T. Souradeep,[17] A. P. Spencer,[23] A. K. Srivastava,[99] A. Staley,[45] M. Steinke,[9] J. Steinlechner,[23,31] S. Steinlechner,[31] D. Steinmeyer,[9,20] B. C. Stephens,[19] R. Stone,[97] K. A. Strain,[23] G. Stratta,[64,65] S. E. Strigin,[56] R. Sturani,[143] A. L. Stuver,[6] T. Z. Summerscales,[144] L. Sun,[132] S. Sunil,[99] P. J. Sutton,[95] B. L. Swinkels,[28] M. J. Szczepańczyk,[33] M. Tacca,[35] D. Talukder,[66] D. B. Tanner,[5] M. Tápai,[111] A. Taracchini,[34] J. A. Taylor,[129] R. Taylor,[1] T. Theeg,[9] E. G. Thomas,[52] M. Thomas,[6] P. Thomas,[43] K. A. Thorne,[6] K. S. Thorne,[58] E. Thrane,[127] S. Tiwari,[15,89] V. Tiwari,[95] K. V. Tokmakov,[118] K. Toland,[23] M. Tonelli,[21,22] Z. Tornasi,[23] C. I. Torrie,[1] D. Töyrä,[52] F. Travasso,[28,40] G. Traylor,[6] D. Trifirò,[10] J. Trinastic,[5] M. C. Tringali,[103,89] L. Trozzo,[145,22] K. W. Tsang,[12] M. Tse,[13] R. Tso,[1] D. Tuyenbayev,[97] K. Ueno,[19] D. Ugolini,[146] C. S. Unnikrishnan,[112] A. L. Urban,[1] S. A. Usman,[95] K. Vahi,[101] H. Vahlbruch,[20] G. Vajente,[1] G. Valdes,[97] N. van Bakel,[12] M. van Beuzekom,[12] J. F. J. van den Brand,[70,12] C. Van Den Broeck,[12] D. C. Vander-Hyde,[41] L. van der Schaaf,[12] J. V. van Heijningen,[12] A. A. van Veggel,[23] M. Vardaro,[48,49] V. Varma,[58] S. Vass,[1] M. Vasúth,[44] A. Vecchio,[52] G. Vedovato,[49] J. Veitch,[52] P. J. Veitch,[77] K. Venkateswara,[140] G. Venugopalan,[1] D. Verkindt,[7] F. Vetrano,[64,65] A. Viceré,[64,65] A. D. Viets,[19] S. Vinciguerra,[52] D. J. Vine,[57] J.-Y. Vinet,[61] S. Vitale,[13] T. Vo,[41] H. Vocca,[39,40] C. Vorvick,[43] D. V. Voss,[5] W. D. Vousden,[52] S. P. Vyatchanin,[56] A. R. Wade,[1] L. E. Wade,[80] M. Wade,[80] R. Walet,[12] M. Walker,[2] L. Wallace,[1] S. Walsh,[19] G. Wang,[15,65] H. Wang,[52] J. Z. Wang,[81] M. Wang,[52] Y.-F. Wang,[87] Y. Wang,[59] R. L. Ward,[24] J. Warner,[43] M. Was,[7] J. Watchi,[91] B. Weaver,[43] L.-W. Wei,[9,20] M. Weinert,[9] A. J. Weinstein,[1] R. Weiss,[13] L. Wen,[59] E. K. Wessel,[11] P. Weßels,[9] T. Westphal,[9] K. Wette,[9] J. T. Whelan,[116] B. F. Whiting,[5] C. Whittle,[127] D. Williams,[23] R. D. Williams,[1] A. R. Williamson,[116] J. L. Willis,[147] B. Willke,[20,9] M. H. Wimmer,[9,20] W. Winkler,[9] C. C. Wipf,[1] H. Wittel,[9,20] G. Woan,[23] J. Woehler,[9] J. Wofford,[116] K. W. K. Wong,[87] J. Worden,[43] J. L. Wright,[23] D. S. Wu,[9] G. Wu,[6] W. Yam,[13] H. Yamamoto,[1] C. C. Yancey,[71] M. J. Yap,[24] Hang Yu,[13] Haocun Yu,[13] M. Yvert,[7] A. Zadrożny,[125] M. Zanolin,[33] T. Zelenova,[28] J.-P. Zendri,[49] M. Zevin,[94] L. Zhang,[1] M. Zhang,[133] T. Zhang,[23] Y.-H. Zhang,[116] C. Zhao,[59] M. Zhou,[94] Z. Zhou,[94] X. J. Zhu,[59] M. E. Zucker,[1,13] and J. Zweizig[1]

(LIGO Scientific Collaboration and Virgo Collaboration)

S. Suvorova,[132,148] W. Moran,[148] and R. J. Evans[132]

[1]*LIGO, California Institute of Technology, Pasadena, California 91125, USA*

[2]*Louisiana State University, Baton Rouge, Louisiana 70803, USA*

[3]*Università di Salerno, Fisciano, I-84084 Salerno, Italy*

[4]*INFN, Sezione di Napoli, Complesso Universitario di Monte S. Angelo, I-80126 Napoli, Italy*

[5]*University of Florida, Gainesville, Florida 32611, USA*
[6]*LIGO Livingston Observatory, Livingston, Louisiana 70754, USA*
[7]*Laboratoire d'Annecy-le-Vieux de Physique des Particules (LAPP), Université Savoie Mont Blanc, CNRS/IN2P3, F-74941 Annecy, France*
[8]*University of Sannio at Benevento, I-82100 Benevento, Italy and INFN, Sezione di Napoli, I-80100 Napoli, Italy*
[9]*Albert-Einstein-Institut, Max-Planck-Institut für Gravitationsphysik, D-30167 Hannover, Germany*
[10]*The University of Mississippi, University, Mississippi 38677, USA*
[11]*NCSA, University of Illinois at Urbana-Champaign, Urbana, Illinois 61801, USA*
[12]*Nikhef, Science Park, 1098 XG Amsterdam, The Netherlands*
[13]*LIGO, Massachusetts Institute of Technology, Cambridge, Massachusetts 02139, USA*
[14]*Instituto Nacional de Pesquisas Espaciais, 12227-010 São José dos Campos, São Paulo, Brazil*
[15]*Gran Sasso Science Institute (GSSI), I-67100 L'Aquila, Italy*
[16]*INFN, Sezione di Roma Tor Vergata, I-00133 Rome, Italy*
[17]*Inter-University Centre for Astronomy and Astrophysics, Pune 411007, India*
[18]*International Centre for Theoretical Sciences, Tata Institute of Fundamental Research, Bengaluru 560089, India*
[19]*University of Wisconsin-Milwaukee, Milwaukee, Wisconsin 53201, USA*
[20]*Leibniz Universität Hannover, D-30167 Hannover, Germany*
[21]*Università di Pisa, I-56127 Pisa, Italy*
[22]*INFN, Sezione di Pisa, I-56127 Pisa, Italy*
[23]*SUPA, University of Glasgow, Glasgow G12 8QQ, United Kingdom*
[24]*Australian National University, Canberra, Australian Capital Territory 0200, Australia*
[25]*Laboratoire des Matériaux Avancés (LMA), CNRS/IN2P3, F-69622 Villeurbanne, France*
[26]*LAL, Université Paris-Sud, CNRS/IN2P3, Université Paris-Saclay, F-91898 Orsay, France*
[27]*California State University Fullerton, Fullerton, California 92831, USA*
[28]*European Gravitational Observatory (EGO), I-56021 Cascina, Pisa, Italy*
[29]*Chennai Mathematical Institute, Chennai 603103, India*
[30]*Università di Roma Tor Vergata, I-00133 Rome, Italy*
[31]*Universität Hamburg, D-22761 Hamburg, Germany*
[32]*INFN, Sezione di Roma, I-00185 Rome, Italy*
[33]*Embry-Riddle Aeronautical University, Prescott, Arizona 86301, USA*
[34]*Albert-Einstein-Institut, Max-Planck-Institut für Gravitationsphysik, D-14476 Potsdam-Golm, Germany*
[35]*APC, AstroParticule et Cosmologie, Université Paris Diderot, CNRS/IN2P3, CEA/Irfu, Observatoire de Paris, Sorbonne Paris Cité, F-75205 Paris Cedex 13, France*
[36]*Korea Institute of Science and Technology Information, Daejeon 34141, Korea*
[37]*West Virginia University, Morgantown, West Virginia 26506, USA*
[38]*Center for Gravitational Waves and Cosmology, West Virginia University, Morgantown, West Virginia 26505, USA*
[39]*Università di Perugia, I-06123 Perugia, Italy*
[40]*INFN, Sezione di Perugia, I-06123 Perugia, Italy*
[41]*Syracuse University, Syracuse, New York 13244, USA*
[42]*University of Minnesota, Minneapolis, Minnesota 55455, USA*
[43]*LIGO Hanford Observatory, Richland, Washington 99352, USA*
[44]*Wigner RCP, RMKI, Konkoly Thege Miklós út 29-33, H-1121 Budapest, Hungary*
[45]*Columbia University, New York, New York 10027, USA*
[46]*Stanford University, Stanford, California 94305, USA*
[47]*Dipartimento di Fisica, Università di Camerino, I-62032 Camerino, Italy*
[48]*Dipartimento di Fisica e Astronomia, Università di Padova, I-35131 Padova, Italy*
[49]*INFN, Sezione di Padova, I-35131 Padova, Italy*
[50]*"Lendulet" Astrophysics Research Group, MTA Eötvös University, Budapest 1117, Hungary*
[51]*Nicolaus Copernicus Astronomical Center, Polish Academy of Sciences, 00-716 Warsaw, Poland*
[52]*University of Birmingham, Birmingham B15 2TT, United Kingdom*
[53]*Università degli Studi di Genova, I-16146 Genova, Italy*
[54]*INFN, Sezione di Genova, I-16146 Genova, Italy*
[55]*RRCAT, Indore MP 452013, India*
[56]*Faculty of Physics, Lomonosov Moscow State University, Moscow 119991, Russia*
[57]*SUPA, University of the West of Scotland, Paisley PA1 2BE, United Kingdom*
[58]*Caltech CaRT, Pasadena, California 91125, USA*
[59]*University of Western Australia, Crawley, Western Australia 6009, Australia*

[60]Department of Astrophysics/IMAPP, Radboud University Nijmegen, P.O. Box 9010, 6500 GL Nijmegen, The Netherlands
[61]Artemis, Université Côte d'Azur, Observatoire Côte d'Azur, CNRS, CS 34229, F-06304 Nice Cedex 4, France
[62]Institut de Physique de Rennes, CNRS, Université de Rennes 1, F-35042 Rennes, France
[63]Washington State University, Pullman, Washington 99164, USA
[64]Università degli Studi di Urbino "Carlo Bo," I-61029 Urbino, Italy
[65]INFN, Sezione di Firenze, I-50019 Sesto Fiorentino, Firenze, Italy
[66]University of Oregon, Eugene, Oregon 97403, USA
[67]Laboratoire Kastler Brossel, UPMC-Sorbonne Universités, CNRS, ENS-PSL Research University, Collège de France, F-75005 Paris, France
[68]Carleton College, Northfield, Minnesota 55057, USA
[69]Astronomical Observatory Warsaw University, 00-478 Warsaw, Poland
[70]VU University Amsterdam, 1081 HV Amsterdam, The Netherlands
[71]University of Maryland, College Park, Maryland 20742, USA
[72]Center for Relativistic Astrophysics and School of Physics, Georgia Institute of Technology, Atlanta, Georgia 30332, USA
[73]Université Claude Bernard Lyon 1, F-69622 Villeurbanne, France
[74]Università di Napoli "Federico II," Complesso Universitario di Monte S. Angelo, I-80126 Napoli, Italy
[75]NASA Goddard Space Flight Center, Greenbelt, Maryland 20771, USA
[76]RESCEU, University of Tokyo, Tokyo 113-0033, Japan
[77]University of Adelaide, Adelaide, South Australia 5005, Australia
[78]Tsinghua University, Beijing 100084, China
[79]Texas Tech University, Lubbock, Texas 79409, USA
[80]Kenyon College, Gambier, Ohio 43022, USA
[81]The Pennsylvania State University, University Park, Pennsylvania 16802, USA
[82]National Tsing Hua University, Hsinchu City, 30013 Taiwan, Republic of China
[83]Charles Sturt University, Wagga Wagga, New South Wales 2678, Australia
[84]University of Chicago, Chicago, Illinois 60637, USA
[85]Pusan National University, Busan 46241, Korea
[86]University of Cambridge, Cambridge CB2 1TN, United Kingdom
[87]The Chinese University of Hong Kong, Shatin, NT, Hong Kong
[88]INAF, Osservatorio Astronomico di Padova, Vicolo dell'Osservatorio 5, I-35122 Padova, Italy
[89]INFN, Trento Institute for Fundamental Physics and Applications, I-38123 Povo, Trento, Italy
[90]Università di Roma "La Sapienza," I-00185 Rome, Italy
[91]Université Libre de Bruxelles, Brussels 1050, Belgium
[92]Sonoma State University, Rohnert Park, California 94928, USA
[93]Montana State University, Bozeman, Montana 59717, USA
[94]Center for Interdisciplinary Exploration & Research in Astrophysics (CIERA), Northwestern University, Evanston, Illinois 60208, USA
[95]Cardiff University, Cardiff CF24 3AA, United Kingdom
[96]Universitat de les Illes Balears, IAC3—IEEC, E-07122 Palma de Mallorca, Spain
[97]The University of Texas Rio Grande Valley, Brownsville, Texas 78520, USA
[98]Bellevue College, Bellevue, Washington 98007, USA
[99]Institute for Plasma Research, Bhat, Gandhinagar 382428, India
[100]The University of Sheffield, Sheffield S10 2TN, United Kingdom
[101]University of Southern California Information Sciences Institute, Marina Del Rey, California 90292, USA
[102]California State University, Los Angeles, 5151 State University Drive, Los Angeles, California 90032, USA
[103]Dipartimento di Fisica, Università di Trento, I-38123 Povo, Trento, Italy
[104]Montclair State University, Montclair, New Jersey 07043, USA
[105]National Astronomical Observatory of Japan, 2-21-1 Osawa, Mitaka, Tokyo 181-8588, Japan
[106]Canadian Institute for Theoretical Astrophysics, University of Toronto, Toronto, Ontario M5S 3H8, Canada
[107]Whitman College, 345 Boyer Avenue, Walla Walla, Washington 99362 USA
[108]School of Mathematics, University of Edinburgh, Edinburgh EH9 3FD, United Kingdom
[109]University and Institute of Advanced Research, Gandhinagar Gujarat 382007, India
[110]IISER-TVM, CET Campus, Trivandrum Kerala 695016, India
[111]University of Szeged, Dóm tér 9, Szeged 6720, Hungary

[112]*Tata Institute of Fundamental Research, Mumbai 400005, India*
[113]*INAF, Osservatorio Astronomico di Capodimonte, I-80131 Napoli, Italy*
[114]*University of Michigan, Ann Arbor, Michigan 48109, USA*
[115]*American University, Washington, D.C. 20016, USA*
[116]*Rochester Institute of Technology, Rochester, New York 14623, USA*
[117]*University of Białystok, 15-424 Biał ystok, Poland*
[118]*SUPA, University of Strathclyde, Glasgow G1 1XQ, United Kingdom*
[119]*University of Southampton, Southampton SO17 1BJ, United Kingdom*
[120]*University of Washington Bothell, 18115 Campus Way NE, Bothell, Washington 98011, USA*
[121]*Institute of Applied Physics, Nizhny Novgorod 603950, Russia*
[122]*Seoul National University, Seoul 08826, Korea*
[123]*Inje University Gimhae, South Gyeongsang 50834, Korea*
[124]*National Institute for Mathematical Sciences, Daejeon 34047, Korea*
[125]*NCBJ, 05-400 Świerk-Otwock, Poland*
[126]*Institute of Mathematics, Polish Academy of Sciences, 00656 Warsaw, Poland*
[127]*The School of Physics & Astronomy, Monash University, Clayton 3800, Victoria, Australia*
[128]*Hanyang University, Seoul 04763, Korea*
[129]*NASA Marshall Space Flight Center, Huntsville, Alabama 35811, USA*
[130]*ESPCI, CNRS, F-75005 Paris, France*
[131]*Southern University and A&M College, Baton Rouge, Louisiana 70813, USA*
[132]*The University of Melbourne, Parkville, Victoria 3010, Australia*
[133]*College of William and Mary, Williamsburg, Virginia 23187, USA*
[134]*Indian Institute of Technology Madras, Chennai 600036, India*
[135]*IISER-Kolkata, Mohanpur, West Bengal 741252, India*
[136]*Scuola Normale Superiore, Piazza dei Cavalieri 7, I-56126 Pisa, Italy*
[137]*Université de Lyon, F-69361 Lyon, France*
[138]*Hobart and William Smith Colleges, Geneva, New York 14456, USA*
[139]*Janusz Gil Institute of Astronomy, University of Zielona Góra, 65-265 Zielona Góra, Poland*
[140]*University of Washington, Seattle, Washington 98195, USA*
[141]*King's College London, University of London, London WC2R 2LS, United Kingdom*
[142]*Indian Institute of Technology, Gandhinagar Ahmedabad Gujarat 382424, India*
[143]*International Institute of Physics, Universidade Federal do Rio Grande do Norte, Natal RN 59078-970, Brazil*
[144]*Andrews University, Berrien Springs, Michigan 49104, USA*
[145]*Università di Siena, I-53100 Siena, Italy*
[146]*Trinity University, San Antonio, Texas 78212, USA*
[147]*Abilene Christian University, Abilene, Texas 79699, USA*
[148]*RMIT University, Melbourne, Victoria 3000, Australia*

[†]Deceased.